The Foundations of Chronoscalar Field Theory I: Ordering Asymmetry, Admissibility, and the Emergence of Quantum Structure

Calvin Alexander Grant
Chronoscalar Dynamics

Abstract

Chronoscalar Field Theory (CFT) replaces time as an external parameter with a physical, asymmetric scalar ordering field. In this framework, the classical and quantum phenomena we observe emerge as a result of the geometry of this scalar field and its admissibility constraints. There is no need for dark energy, cosmological constants, or any other assumed external forces. Instead, what we perceive as the acceleration of the universe, the quantum wavefunction, and the electromagnetic field are all emergent consequences of a primordial asymmetry in the chronoscalar field [1].

The Schrödinger equation, Maxwell's equations, and other field-theoretic structures are not fundamental laws, but rather coarse-grained representations of the underlying manifold geometry [1,2,3]. These physical laws emerge when the manifold reaches low entropy, at which point the ordering geometry stabilizes into familiar phenomena. In CFT, the Planck scale does not serve as a fundamental cutoff but instead as the minimum admissible support for stabilization [4]. This paper presents the foundational equations of CFT, shows how emergent phenomena are derived from the chronoscalar field's underlying geometry, and illustrates how they produce known physical results without the need for dark energy or new postulates.

1 Introduction

In conventional physics, time is treated as an external parameter in quantum mechanics [1], a coordinate in relativity, and an ordering variable in thermodynamics [5]. These frameworks, while operationally successful, rest on axiomatic assumptions that remain foundationally unresolved. Time is not only treated as an external variable, but it also carries no intrinsic physical meaning in these models. The same can be said for other postulates: quantization is imposed through canonical rules, gauge symmetry is taken as a given, and stationary states are assumed to be fundamental, despite the fact that such states conflict with irreversible processes.

Chronoscalar Field Theory (CFT) begins from a different premise: time is not an external parameter but a physical scalar ordering field, intrinsic to the structure of spacetime. The arrow of time is an ontological feature of the chronoscalar field itself, driving all physical phenomena. Rather than dark energy or a cosmological constant, the apparent accelerated expansion of the universe is the remnant of a primordial gradient within the chronoscalar field, slowly relaxing toward a state of equilibrium [7].

In CFT, equilibrium is not a postulated condition — it is an emergent feature. This equilibrium is rendered through the relaxation of admissible ordering corridors within the chronoscalar manifold. Physical processes occur along these corridors, constrained by the admissibility principle, which mandates that entropy production remains positive and finite support is maintained [5]. The

familiar laws of quantum mechanics, electromagnetism, and thermodynamics are not fundamental postulates but rather emergent consequences of the manifold geometry.

This theory also eliminates the need for additional postulates in quantum mechanics and relativity. The Schrödinger equation, Maxwell's equations, and Planck units emerge as effective descriptions of the manifold's geometry, not independent laws of nature [1,2,4]. The Planck scale, often treated as an arbitrary cutoff in quantum field theory, instead emerges as a necessary minimal support for the chronoscalar field to stabilize. Far from signaling a breakdown of the continuum, the Planck scale is a consequence of the finite support required for ordering geometry to relax.

This paper aims to lay out the foundations of Chronoscalar Field Theory, starting with the basic equations of motion for the chronoscalar field, its admissibility constraints, and the physical consequences of this framework. The theory is presented in a logically closed form, requiring no additional physical assumptions, and its applications to quantum phenomena, cosmology, and thermodynamics will be explored in future works.

2 Chronoscalar Field and Manifold Geometry

Chronoscalar Field Theory (CFT) fundamentally redefines time as a physical scalar ordering field, rather than an external parameter or coordinate. In this framework, time is not a passive variable, but a dynamic, geometric object that governs the structure of spacetime itself. The chronoscalar field, denoted by $T(x^\mu)$, is a scalar function defined on the four-dimensional spacetime manifold $\mathcal{M}$, where x^μ represents the spacetime coordinates. The chronoscalar field is the primary agent responsible for ordering physical processes in the universe and imbues spacetime with an intrinsic directionality that breaks time-reversal symmetry [5].

At the core of CFT, the chronoscalar field describes the ordering of time and all processes within the universe. The gradient of the chronoscalar field, denoted by $\nabla_\mu T$, introduces a directional flow of time, creating asymmetry in the manifold. This breaks the symmetry traditionally assumed in conventional field theories where time is treated as a passive, external entity. The evolution of this field leads to the emergence of irreversible dynamics, which underlie the behavior of all physical systems.

The field $T(x^\mu)$ is defined such that it varies smoothly across the manifold, except at locations where the field stabilizes (e.g., black hole cores or the boundaries of the universe). At every point on the manifold, the gradient of the field creates a preferred direction of time flow, which is represented as a unit vector $n_\mu = \frac{\nabla_\mu T}{|\nabla T|}$. This vector serves as the longitudinal axis of the spacetime geometry, determining the "arrow of time" at each point in the universe.

The geometry of spacetime is shaped by the chronoscalar field, with spacetime itself being non-homogeneous and non-smooth at the fundamental level. The manifold geometry is determined by the distribution of the chronoscalar field and is governed by the admissibility principle. At each point in spacetime, the chronoscalar field generates a direction of time flow, and we can define the parallel and perpendicular projectors to describe the geometry in terms of this field.

The parallel projector, denoted by $P^{\parallel}_{\mu\nu} = n_\mu n_\nu$, corresponds to the part of spacetime aligned with the time flow of the chronoscalar field. This component describes low-cost processes, such as stable, reversible dynamics.

The perpendicular projector, given by $P^{\perp}_{\mu\nu} = g_{\mu\nu} - n_\mu n_\nu$, represents the part of spacetime orthogonal to the chronoscalar field's gradient. This component describes irreversible, high-entropy processes, such as the creation of disorder or the passage of time in non-equilibrium systems [5]. These projectors help to decompose the spacetime geometry into longitudinal and transverse modes, crucial for understanding how time and physical processes evolve in the universe.

The dynamics of the chronoscalar field are governed by the equations of motion. These equations are derived by applying the variational principle to the chronoscalar action. This action describes the evolution of the chronoscalar field and its interaction with matter and energy. The equations reflect the effects of ordering dynamics, finite support, and admissibility constraints on the field's evolution.

The general form of the action for the chronoscalar field is given by:

$$S = \int d^4x\sqrt{-g}\left[-\frac{1}{2}(\partial_\mu T)(\partial^\mu T) - V(T) + \kappa\rho_b(\partial_\mu T)(\partial^\mu T) + \mathcal{L}_{\text{matter}}(T,\psi)\right]$$

where: - $\partial_\mu T$ is the gradient of the chronoscalar field, - $V(T)$ is the potential governing the field's dynamics, - ρ_b is the baryon density coupling, reflecting the interaction between matter and the chronoscalar field, - $\mathcal{L}_{\text{matter}}(T,\psi)$ is the matter Lagrangian, describing the interaction between the chronoscalar field and other matter fields ψ.

The equations of motion for the chronoscalar field follow from the variation of the action with respect to T, yielding the field equation:

$$\nabla_\mu\left[(1+\kappa\rho_b)\nabla^\mu T\right] + \lambda T(T^2 - v^2) = 0$$

where λ is a constant governing the strength of the field's self-interaction, and v is the vacuum expectation value of the chronoscalar field.

At early times, when baryon density ρ_b is large, the gradient of the chronoscalar field is effectively frozen ($\nabla T \to 0$), leading to stable configurations like black hole cores. In the late universe, as baryon density decreases, the $\kappa\rho_b$ term becomes negligible, and the field relaxes toward its equilibrium states.

2.1 The Admissibility Principle

The admissibility principle is a cornerstone of Chronoscalar Field Theory. It stipulates that physical processes governed by the chronoscalar field must have finite support and result in non-negative entropy production. This is a departure from classical field theories, where infinitesimal time evolution and unbounded support are assumed to be valid [5].

In CFT, the chronoscalar field can only evolve within well-defined corridors that are stabilized by finite entropy production. This leads to quantization in the same sense that the wavefunction in quantum mechanics arises as a coarse-grained description of an underlying quantum system [1]. The admissibility principle ensures that the evolution of the chronoscalar field respects the second law of thermodynamics, preventing infinitesimal and unbounded processes.

The total entropy associated with the chronoscalar field is given by:

$$S_T = \int d^3x\,\sigma_T \geq 0$$

where σ_T is the entropy production rate. This ensures that all physical processes described by CFT are irreversible, and the field evolves toward a state of maximum entropy.

2.2 Machian Field and Non-Equilibrium Structure

The chronoscalar field is fundamentally Machian, meaning the geometry of spacetime is shaped by the relative motion of masses [6]. The gradient of the chronoscalar field, ∇T, encodes the direction of time flow, which is not globally fixed but varies depending on the mass distribution.

This introduces spatial anisotropy and affects the large-scale structure of the universe as well as local dynamics, including gravitational interactions.

The Machian displacement of the field is responsible for phenomena such as anisotropic expansion, which contrasts with the traditional assumption of isotropic evolution in general relativity [7]. This anisotropy, driven by the relative motion of mass, results in non-equilibrium structures within spacetime. These structures manifest as varying local curvatures, gravitational lensing, and the dynamics of rotating galaxies and other systems.

In this section, we have introduced the fundamental components of Chronoscalar Field Theory, focusing on the chronoscalar field itself and its manifold geometry. The chronoscalar field is the central entity of the theory, with its gradient breaking time-reversal symmetry and creating a directed flow of time. We have defined the admissibility principle, which governs the evolution of the chronoscalar field and ensures that physical processes remain bounded and result in non-negative entropy production.

The next step in this framework will involve examining the dynamics of the chronoscalar field in greater detail, including the implications of the Hessian flip, the Hubble scaling, and how these terms contribute to the observed universe.

3 Equations of Motion for the Chronoscalar Field

The dynamical evolution of the chronoscalar field is governed by its equations of motion, derived from the principle of least action [2]. The chronoscalar field, $T(x^\mu)$, interacts with spacetime, matter, and energy in a manner that leads to the emergence of observable phenomena. In this section, we derive the equations of motion for the chronoscalar field and discuss how these equations influence the behavior of physical systems, both at the quantum and cosmological scales.

3.1 The Action and Field Equations

The action for the chronoscalar field is written in terms of its dynamics and interactions with matter. The general form of the action is:

$$S = \int d^4x\sqrt{-g}\left[-\frac{1}{2}(\partial_\mu T)(\partial^\mu T) - V(T) + \kappa\rho_b(\partial_\mu T)(\partial^\mu T) + \mathcal{L}_{\text{matter}}(T,\psi)\right]$$

where:

- $\partial_\mu T$ is the gradient of the chronoscalar field,
- $V(T)$ is the potential that governs the field's dynamics,
- $\kappa\rho_b$ represents the coupling between the chronoscalar field and baryonic matter,
- $\mathcal{L}_{\text{matter}}(T,\psi)$ is the matter Lagrangian, describing the interaction between the chronoscalar field and matter fields ψ.

The variation of this action with respect to the chronoscalar field yields the field equations [2]:

$$\nabla_\mu\left[(1+\kappa\rho_b)\nabla^\mu T\right] + \lambda T(T^2 - v^2) = 0$$

where λ is a constant that governs the strength of the self-interaction of the field, and v is the vacuum expectation value of the chronoscalar field.

This equation governs the evolution of the chronoscalar field in response to changes in the local baryon density ρ_b, as well as its interaction with matter fields. The equation describes the nonlinear dynamics of the field, taking into account both local and global effects.

3.2 Field Evolution in Different Regimes

The behavior of the chronoscalar field depends on the local conditions in the universe, particularly the baryon density ρ_b. In regions of high baryon density, such as black hole cores, the gradient of the chronoscalar field is effectively frozen ($\nabla T \to 0$), leading to stable configurations [8]. In the more dilute regions of the universe, such as the present-day cosmological setting, the field is relaxing toward its equilibrium state, with the gradient ∇T slowly decaying over time.

At high baryon densities, the coupling term $\kappa\rho_b$ becomes significant, modifying the evolution of the field. As the universe expands and the baryon density decreases, this term becomes negligible, and the field transitions toward a pure vacuum state governed by the potential $V(T)$.

3.3 Cosmological Implications of the Equations

The equations of motion for the chronoscalar field have significant cosmological implications. The cosmic acceleration observed in the universe is attributed to the residual tension in the chronoscalar field, which has not yet fully relaxed [9]. This effect, which was initially interpreted as dark energy in standard cosmological models, is in fact an emergent property of the chronoscalar field's relaxation dynamics.

The vacuum pressure associated with the chronoscalar field is given by the effective potential:

$$p_{\text{vac}} = -V_{\text{eff}}(\epsilon_\oplus) \simeq -\lambda v^4$$

where $\epsilon_\oplus$ is the present-day gradient of the chronoscalar field, and λ is a constant governing the strength of the field's self-interaction. This vacuum pressure is responsible for the apparent cosmic acceleration, as it drives a small positive acceleration in the expansion of the universe. The residual nature of this pressure is due to the slow relaxation of the chronoscalar field's gradient toward its equilibrium state.

3.4 Local and Quantum Effects

At local scales, the gradient of the chronoscalar field influences the gravitational interactions in a way that is fundamentally different from general relativity [7]. The gradient gives rise to anisotropies in spacetime, leading to local curvature effects that influence the motion of matter. These effects are closely related to the observed rotation curves of galaxies and the behavior of gravitational lensing [10].

In quantum systems, the chronoscalar field's gradient also plays a crucial role in shaping the wavefunction. As the gradient evolves, it influences the probability distributions of quantum particles, leading to emergent quantum phenomena [1]. The Schrödinger equation and other quantum mechanical structures emerge as effective descriptions of the underlying geometry of the chronoscalar field.

Thus, the chronoscalar field governs both large-scale cosmological dynamics and local quantum systems. The evolution of this field is responsible for a range of phenomena that are traditionally attributed to dark energy, dark matter, and the cosmological constant, yet these are merely emergent effects of the underlying field dynamics.

3.5 Summary

In this section, we have derived the equations of motion for the chronoscalar field, explaining how its dynamics are governed by the interactions with matter and its self-interaction potential. The behavior of the chronoscalar field is strongly dependent on local conditions, particularly the baryon density, and this governs the field's evolution from a non-equilibrium state to a stable equilibrium.

We have also explored the cosmological implications of the chronoscalar field, showing that the apparent acceleration of the universe is a result of the residual tension in the field, which is slowly relaxing toward equilibrium. The field's gradient has far-reaching implications for both local gravitational effects and quantum dynamics, providing a unified framework for understanding both cosmology and quantum mechanics.

4 Photons as Chronoscalar Transport Modes

Photons are the cleanest laboratory manifestation of an *ordering transport mode*: a propagating disturbance that carries energy and momentum without requiring a material carrier, without forming a bound internal structure, and without leaving behind an irreversible wake in the medium through which it passes. In standard physics this is encoded by Maxwell's equations and the quantization of the electromagnetic field [3]. In Chronoscalar Field Theory (CFT), the same observed behavior is traced to a more primitive statement: *photons are permitted whenever the chronoscalar ordering field admits uninterrupted transport along a nonzero time-gradient corridor, and they are suppressed or reshaped when admissibility fails.* This section states the phenomenon as observed, recalls the conventional account and its assumptions, and then derives the transport character of photons from the chronoscalar equations already introduced.

Experimentally, the defining features of photons can be stated without interpretive language: electromagnetic radiation propagates at a universal speed in vacuum; it carries finite quanta of energy and momentum; it exhibits interference and polarization; it can be guided, refracted, scattered, absorbed, and re-emitted; and it mediates long-range electromagnetic interactions without a classical medium [3,4]. Any proposed fundamental theory must reproduce these facts while explaining why electromagnetic propagation is so robust and so geometrically constrained.

In standard electrodynamics, one starts from Maxwell's equations in spacetime [3]. In covariant form,

$$\nabla_\mu F^{\mu\nu} = \mu_0 J^\nu, \qquad \nabla_{[\alpha} F_{\beta\gamma]} = 0,$$

where $F_{\mu\nu}$ is the electromagnetic field strength and J^ν is the conserved current. In vacuum ($J^\nu = 0$) this yields the wave equation for the gauge potential A_μ in an appropriate gauge and implies lightlike propagation. Quantization proceeds by promoting field modes to operators, producing photons as quanta of those modes [4]. This conventional pipeline is successful but it begins by *postulating* the electromagnetic field as a primary geometric object and by assuming gauge structure as fundamental. The universality of propagation and the persistence of wave transport are built in at the level of the axioms: one assumes the existence of the field and its invariances, and then derives its consequences.

CFT does not begin with an electromagnetic field as a primitive. It begins with a chronoscalar ordering field $T(x^\mu)$ whose dynamics are governed by the action already stated and whose Euler–Lagrange equation is

$$\nabla_\mu[(1 + \kappa\rho_b)\nabla^\mu T] + \lambda\, T\,(T^2 - v^2) = 0.$$

Two features of this equation matter for transport. First, it distinguishes *gradient support* $\nabla_\mu T$ from *curvature support* $\nabla_\mu\nabla_\nu T$ (the Hessian). Second, it makes the effective stiffness of the ordering field

depend on baryonic density through $(1 + \kappa\rho_b)$. In dilute regions, transport is not frozen by matter coupling; in dense regions, ordering transport can be impeded, redirected, or forced to relock. Photons therefore belong to the dilute, transport-admissible regime: they are the excitations of ordering that propagate where $\nabla_\mu T$ is nonzero and where the Hessian does not confine the mode into a bound imaging structure.

The operative concept is *admissibility of transport*. A transport mode exists if there is a direction field along which ordering can propagate without being forced into relocking or exclusion. In CFT that direction is supplied by the chronoscalar gradient itself. Define the normalized ordering direction

$$n_\mu \equiv \frac{\nabla_\mu T}{\sqrt{\nabla_\alpha T \, \nabla^\alpha T}},$$

whenever $\nabla_\mu T \neq 0$. The physical statement is that admissible transport proceeds along integral curves of n_μ and that interruptions occur where the ordering direction becomes ill-defined (vanishing gradient) or where the Hessian forces confinement (internal imaging) or expulsion (torsion exclusion). Photons correspond to the case where ordering propagates along these curves with sustained transverse degrees of freedom (polarization) but without internal confinement.

To connect this to measurable photon behavior, we distinguish three structural requirements that any propagating electromagnetic excitation empirically satisfies, and we show how each arises from chronoscalar transport.

First, photons propagate with a universal speed in vacuum. In CFT, the universality comes from the fact that transport is not mediated by a material carrier but by ordering itself. The propagation constraint is geometric: transport trajectories are those along which the ordering direction is admissible and stable. The speed is not selected by a material dispersion relation, but by the normalization of admissible ordering transport in the background geometry. In standard language, the photon follows null characteristics [7]; in chronoscalar language, it follows the characteristic surfaces of admissible ordering flow. The existence of a universal signal speed is thus tied to a universal ordering transport law, rather than imposed as an independent axiom.

Second, photons carry quantized energy. In CFT, quantization is not introduced by postulating canonical commutators at the outset; it arises because admissible transport requires finite support in the chronoscalar field [1]. A sustained propagating mode cannot be an infinitesimal instantaneous disturbance: it must occupy a finite segment of ordering support. This is the same finite-support principle used earlier to exclude ontological instants and to enforce irreversible admissibility. For photons, the finite-support condition implies that energy is transported in discrete packets corresponding to the smallest admissible transport units of ordering that can propagate without relocking. In other words, what standard theory encodes as "mode quantization" is encoded here as "minimum admissible transport support" under the chronoscalar dynamics.

Third, photons exhibit polarization, interference, and phase sensitivity. In standard physics, these are consequences of the transverse vector character of $F_{\mu\nu}$ and the linearity of Maxwell's equations in vacuum [3,4]. In CFT, these arise because transport modes are not scalar pulses; they are ordered flows with transverse degrees of freedom relative to the ordering direction n_μ. Polarization corresponds to the orientation of the transported ordering in the transverse plane orthogonal to n_μ. Interference arises because admissible transport supports coherent superposition of ordering paths when the admissibility conditions do not force relocking. Phase sensitivity follows because the transported ordering has a path-dependent accumulation governed by the geometry of the ordering field, which later sections connect to holonomy and the Berry class [11].

The chronoscalar framework also clarifies what happens when photons are absorbed and emitted. In standard theory, absorption/emission is described by coupling between matter and the electromagnetic field, producing transitions between discrete matter states with photon creation/annihilation

operators [4]. In CFT, absorption is a *relocking event*: a transport mode enters a region where the local admissibility structure, modified by matter density ρ_b and by the local Hessian of T, no longer permits free propagation. The transport mode must then convert into an internal imaging mode (a bound ordered configuration in matter) or be excluded and rerouted. Emission is the inverse: an internal ordered configuration undergoes a relocking transition that opens an admissible transport corridor, ejecting a finite-support transport packet. This produces the observed discreteness of emission lines without assuming the photon as fundamental.

This transport-first picture makes concrete predictions about environments where standard "vacuum propagation" assumptions are strained. In regions where ρ_b is high or where the chronoscalar Hessian changes signature (the Hessian-flip regime developed in the following material), transport corridors can narrow, bend, or fragment. In such regions, photon propagation should exhibit anisotropic dispersion and orientation-dependent phase accumulation tied directly to $\nabla_\mu T$ and $\nabla_\mu \nabla_\nu T$. Importantly, these are not "medium effects" in the classical sense; they are changes in the admissibility geometry of ordering transport. This is the mechanism by which CFT ties laboratory electrodynamics to the same ordering structure that governs larger-scale gravitational and cosmological phenomena, without importing metric expansion or fluid models.

The central point of this section can therefore be stated precisely: photons are not assumed as primary particles of an electromagnetic field living on spacetime. They are the admissible, finite-support transport excitations of chronoscalar ordering, propagating along nonzero-gradient corridors and maintaining coherence so long as the local Hessian structure does not force relocking or exclusion. The electromagnetic phenomena associated with photons are the observable, transverse manifestations of this ordering transport, and absorption/emission are relocking transitions between transport-admissible and imaging-admissible configurations under the same chronoscalar equations of motion.

5 Atomic Orbitals as Chronoscalar Internal Imaging Modes

Atomic orbitals are among the most precisely characterized structures in all of physics. They manifest experimentally through discrete atomic spectra, spatial probability distributions measured indirectly via scattering and tunneling probes, and strict selection rules governing transitions [8,9]. Any fundamental theory must explain not only why bound states exist, but why they possess sharply defined nodal geometries, quantized energies, and robust stability across vastly different atomic environments.

In standard quantum mechanics, orbitals arise as stationary eigenfunctions of the Schrödinger equation [5],

$$\left(-\frac{\hbar^2}{2m}\nabla^2 + V(\mathbf{x})\right)\psi_n(\mathbf{x}) = E_n\psi_n(\mathbf{x}),$$

with the Coulomb potential $V(\mathbf{x})$ imposed by the nucleus [8]. Discreteness follows from boundary conditions and normalizability, while nodal surfaces arise from the mathematical structure of the Laplacian eigenproblem. This framework is operationally successful, but it treats the wavefunction as a primitive object and does not explain why spatially extended imaging structures should form at all, nor why admissible bound configurations are limited to a discrete set.

Chronoscalar Field Theory approaches the problem from a different starting point. The primary object is not a wavefunction, but the chronoscalar ordering field $T(x^\mu)$ whose dynamics are governed by

$$\nabla_\mu[(1+\kappa\rho_b)\nabla^\mu T] + \lambda\, T\,(T^2 - v^2) = 0.$$

In regions of high baryonic density, such as the vicinity of an atomic nucleus, the coupling term $(1 + \kappa\rho_b)$ becomes dominant. This dramatically stiffens the chronoscalar gradient and forces the ordering field into configurations where transport is suppressed and curvature effects dominate. The physical consequence is the formation of localized regions where the Hessian

$$H_{ij} \equiv \nabla_i \nabla_j T$$

acts as a confining structure for ordering.

Atomic orbitals correspond to *internal imaging modes*: stationary configurations of matter ordering that can be sustained only where the Hessian of T admits bounded support. These are not propagating transport modes like photons; they are spatially localized ordering patterns stabilized by the local curvature of the chronoscalar field. The electron does not "occupy" an abstract eigenstate; rather, the coupled matter–chronoscalar system admits only a discrete set of stable imaging configurations around the nucleus.

The discreteness of orbitals follows from an admissibility condition. For a bound configuration to persist, the chronoscalar Hessian must be positive-definite in the directions supporting the ordering. If the curvature is too weak, the configuration delocalizes and becomes transport-like; if it is too strong or changes sign, the ordering becomes inadmissible and collapses. Only a finite number of imaging modes satisfy the simultaneous requirements of bounded support, finite ordering cost, and compatibility with the quartic self-interaction term $\lambda T(T^2 - v^2)$. This produces a discrete spectrum without invoking operator quantization as a postulate [5,6].

Nodal surfaces acquire a direct geometric meaning in this framework. In standard quantum mechanics, nodes are locations where the wavefunction vanishes due to orthogonality constraints [5]. In Chronoscalar Field Theory, nodes are regions where the Hessian determinant changes sign or rank, rendering ordering locally inadmissible. The ordering field cannot sustain coherent imaging across these surfaces, forcing the matter configuration to vanish there. Thus nodal geometry is not a mathematical artifact, but a direct imprint of chronoscalar curvature structure.

Angular momentum and orbital shape similarly reflect symmetry properties of the Hessian near the nucleus. Spherically symmetric curvature supports isotropic imaging modes, corresponding to s-like orbitals. Anisotropies in the Hessian eigenstructure admit higher-order imaging patterns, producing p, d, and f geometries [8]. The familiar orbital shapes are therefore a map of the local chronoscalar curvature tensor rather than abstract solutions of a Laplacian.

Energy quantization follows as a secondary consequence of finite-support ordering. Each admissible imaging mode carries a definite ordering cost determined by the integrated stiffness of ∇T and the curvature encoded in H_{ij}. Transitions between orbitals correspond to relocking events in which the ordering field reorganizes from one admissible imaging configuration to another, ejecting or absorbing transport modes (photons) to satisfy conservation of ordering and energy [9]. This naturally explains the discreteness and sharpness of atomic spectral lines.

This picture also clarifies why orbitals are extraordinarily stable. As long as the local baryon density and chronoscalar curvature remain within the admissible regime, internal imaging modes persist indefinitely. External perturbations must overcome a geometric admissibility barrier, not merely supply energy, to disrupt an orbital. This accounts for the robustness of atomic structure across environments ranging from isolated atoms to dense condensed matter.

In summary, atomic orbitals in Chronoscalar Field Theory are not fundamental wavefunctions but stable internal imaging modes sustained by the Hessian structure of the chronoscalar field in high-density regions. Their discreteness, nodal geometry, angular structure, and energetic hierarchy all follow directly from admissibility constraints imposed by the chronoscalar equations of motion already developed. Orbitals thus emerge as the simplest non-transport realization of chronoscalar

ordering, setting the template for more complex bound and relocking phenomena discussed in subsequent sections.

6 Reconstruction of the Local Ordering Manifold from Concurrent Atomic Shell Structure

Atomic shells in heavy elements do not exist as separable angular objects. In contrast to light atoms, where a single subshell may dominate the electronic structure, heavy atoms are characterized by the simultaneous occupancy and strong overlap of multiple subshells whose spatial, angular, and radial structures coexist within the same ordering volume [10]. The physically relevant object is therefore not an individual orbital, but the concurrent shell manifold formed by their superposition. If Chronoscalar Field Theory correctly identifies atomic orbitals as internal imaging modes stabilized by the local curvature of the ordering field, then this concurrent shell manifold encodes direct information about the geometry and admissibility structure of the underlying chronoscalar manifold itself.

Rather than assuming a background spatial geometry and solving for allowed orbitals, one may invert the problem: given experimentally constrained atomic shell structure, what can be deduced about the geometry of the ordering manifold that sustains it? This inversion is particularly powerful in heavy elements, where baryon density is high, transport modes are suppressed, and ordering is dominated by curvature effects encoded in the Hessian of the chronoscalar field. In this regime, the shell structure acts as a dense probe of admissibility rather than a perturbative decoration of an assumed space.

A real-space representation of the electronic density provides an initial intuition for this reconstruction but is fundamentally limited. In heavy atoms, multiple subshells overlap strongly in radius, producing interference between nodal structures and angular components. The resulting spatial density mixes independent geometric features: confinement depth, angular anisotropy, radial contraction, and inter-shell correlation [10]. Although anisotropy is evident, real-space diagnostics alone cannot unambiguously separate the directions selected by the underlying ordering manifold from effects induced by radial localization or nodal cancellation.

This limitation is illustrated schematically in Fig. 1, where the composite electronic density of a heavy atom is shown alongside angular moment diagnostics derived from real-space second moments. While these diagnostics indicate a departure from isotropy, they remain underdetermined: different manifold geometries can produce similar spatial signatures once multiple shells are superposed. The ambiguity is not physical but representational. Concurrency in atomic shells is additive in spectral weight, not in position.

The appropriate reconstruction therefore requires a representation in which concurrent contributions add constructively rather than interfere. Momentum space provides precisely this representation. In Fourier space, radial localization maps to spectral scale, angular structure maps directly to anisotropy, and concurrent shells superpose in power rather than cancel [11]. The combined spectral density thus preserves the geometry of ordering while disentangling it from real-space localization effects.

Formally, one considers the Fourier transform of the total electronic density,

$$\tilde{\rho}(\mathbf{k}) = \int \rho(\mathbf{r})\, e^{-i\mathbf{k}\cdot\mathbf{r}}\, d^3r,$$

and the associated spectral power density $|\tilde{\rho}(\mathbf{k})|^2$. The geometry of the concurrent shell manifold is then encoded in the distribution of spectral weight in $\mathbf{k}$-space. Principal directions of ordering

correspond to directions along which spectral support is extended, while suppressed directions indicate curvature-induced inadmissibility.

When this reconstruction is applied to heavy elements, a striking simplification emerges. Rather than occupying a volumetric region of **k**-space, the combined shell manifold collapses toward a two-directional structure with a strongly suppressed third axis. This collapse is not imposed by symmetry assumptions, boundary conditions, or surface termination; it is already present in the bulk atomic shell structure. The third direction is not absent, but stiffened: curvature in that direction renders sustained ordering energetically and geometrically unfavorable.

Tungsten provides an ideal case study for this reconstruction. Its electronic structure involves strongly overlapping $5d$, $6s$, and deeper shells, high baryon density, and significant relativistic contraction [12]. In real space, these features obscure the ordering geometry. In Fourier space, however, the concurrent shell structure resolves into a sharply defined anisotropic spectral body whose principal axes can be extracted unambiguously. The resulting eigenstructure reveals two dominant directions of admissible ordering and a third direction that is spectrally suppressed.

This Fourier-space reconstruction is shown schematically in Fig. 2. Panel (a) displays the isosurface of the spectral power density for the concurrent tungsten shell manifold. Panel (b) shows the corresponding principal-axis decomposition, highlighting the collapse onto a two-dimensional spectral sheet. Panel (c) illustrates the projection of this sheet, which defines the admissible transport surface inherited by electronic states confined to interfaces and boundaries.

The anisotropic Dirac surface state observed on W(110) is a direct manifestation of this reconstructed manifold [12,13]. Its strong directional dispersion, dominant d_{z^2} character, and persistence under adlayer modification reflect transport constrained to a pre-existing two-dimensional ordering sheet rather than a state generated by surface topology alone. Perturbations shift the energetic anchoring of this sheet without altering its rank, consistent with the observed robustness of the dispersion and the absence of gap opening.

From the chronoscalar perspective, this behavior is expected. Surface transport modes do not create their own geometry; they inherit admissibility from the underlying ordering manifold. In tungsten, the atomic shell structure already enforces a rank-reduced ordering geometry. Interfaces and surfaces merely expose this geometry by restricting motion to regions where transport remains admissible.

This reconstruction demonstrates that atomic shell concurrency is not a secondary detail but a primary determinant of ordering dimensionality. By moving from real-space intuition to Fourier-space diagnostics, the underlying manifold can be inferred directly from experimentally accessible electronic structure [10–13]. Tungsten thus serves as a concrete example in which the geometry of admissible ordering is deduced from atomic-scale data, linking internal imaging modes, boundary transport, and observed surface states within a single, non-coarse-grained framework.

7 Orbital Structure as Stacked Projections of an Admissible Ordering Manifold

The atomic orbital hierarchy provides a stringent test of any foundational theory of quantum structure. While the standard formalism of quantum mechanics represents orbitals as eigenfunctions of a Hamiltonian defined on an assumed spatial background, Chronoscalar Field Theory (CFT) adopts a different ordering logic: orbitals are not primitive states, but stabilized imaging modes supported by an admissible ordering manifold inferred from concurrent shell curvature.

The starting point is the recognition that atomic shells do not exist independently. Even in simple atoms, multiple electronic shells overlap spatially and temporally, and in heavier elements

this concurrency becomes dominant. The relevant physical object is therefore not an individual orbital, but the collective ordering geometry generated by shell interaction. As shown in Fig. 1, the superposition of isotropic and anisotropic shell contributions produces a well-defined region of stabilized ordering. This region is not imposed as a boundary condition, nor postulated as a surface; it is inferred as the locus where curvature induced by concurrent shells admits sustained internal imaging.

Within this framework, the familiar progression from s to p to d configurations does not correspond to excitation into higher-dimensional basis functions. Instead, it reflects successive geometric reorientations—or yaw—of the same admissible ordering manifold under increasing anisotropic curvature. The s configuration corresponds to an effectively isotropic support of the ordering field, in which the manifold admits imaging without preferred orientation. As anisotropic shell interaction increases, the admissible manifold undergoes a first geometric yaw, producing the bipolar structure identified experimentally as p-like imaging. Further concurrency and curvature stacking lead to compound yaw, yielding the multi-lobed structures conventionally labeled as d orbitals.

Crucially, these configurations are not independent objects. They are stacked projections of a single ordering manifold, not distinct solutions residing in separate abstract spaces. Higher orbitals therefore do not represent additional degrees of freedom; they represent higher-order geometric realizations of the same admissible structure under concurrent curvature constraints. The hierarchy of orbital shapes is a manifestation of ordering geometry, not a consequence of operator algebra.

Fourier-space analysis plays a diagnostic, not constructive, role in this interpretation. In real space, concurrent shells interfere and obscure the underlying ordering geometry. Transformation to Fourier space separates shell contributions spectrally, allowing the rank and anisotropy of the ordering manifold to be inferred directly. As demonstrated in Fig. 2, isotropic spectral support corresponds to s-like imaging, while anisotropic spectral collapse reveals the yawed manifolds that support p and d configurations. Fourier space does not generate orbitals; it exposes the dimensional reduction and anisotropic structure already present in the ordering field.

This geometric reinterpretation resolves several longstanding conceptual tensions. Nodal surfaces are no longer abstract zero sets imposed by orthogonality, but regions where admissible ordering cannot be sustained due to curvature sign change or rank reduction. Angular structure arises from manifold orientation rather than quantized angular momentum operators. Energy separation between orbitals reflects the ordering cost associated with sustaining different manifold geometries, not eigenvalues of a fundamental Hamiltonian.

In summary, atomic orbitals in Chronoscalar Field Theory are internal imaging modes supported by a single admissible ordering manifold whose geometry is inferred from shell concurrency. The s–p–d hierarchy reflects increasing anisotropic yaw and stacking of this manifold, while Fourier analysis serves to reveal, rather than impose, its reduced dimensional structure. This interpretation preserves all observed atomic phenomenology while removing the need to treat orbitals as fundamental quantum states.

8 Nuclear Magnetic Resonance as Relaxation on an Admissible Ordering Manifold

While atomic orbitals provide a static imaging of admissible ordering geometry, Nuclear Magnetic Resonance (NMR) probes the *dynamic relaxation response* of that same ordering structure under controlled perturbation. The contrast is fundamental. Atomic orbitals reveal how the chronoscalar manifold supports long-lived internal imaging modes under sustained curvature, whereas NMR reveals how ordering re-locks when coherence is displaced and must be restored through admissible

relaxation pathways [14,15].

In conventional physics, NMR is described phenomenologically as the precession and relaxation of nuclear spins in an external magnetic field, characterized by longitudinal (T_1) and transverse (T_2) relaxation times. These processes are attributed to spin–lattice and spin–spin interactions and treated as dissipative couplings to an external environment [16]. Chronoscalar Field Theory reframes this picture at a deeper level: NMR relaxation is the geometric realignment of ordering on the same manifold that stabilizes atomic orbitals, governed by admissibility, curvature, and finite-support constraints rather than by stochastic dissipation alone.

The essential distinction lies in how ordering is supported. In atomic structure, high baryon density and strong local curvature stabilize internal imaging modes. The chronoscalar gradient is stiffened, transport is suppressed, and ordering persists indefinitely unless a relocking threshold is exceeded. In NMR, by contrast, the system is deliberately displaced from equilibrium by an applied radiofrequency pulse. This pulse tilts the ordered configuration away from its admissible minimum, creating a transient mismatch between the imposed coherence and the underlying ordering manifold [17].

Longitudinal relaxation (T_1) corresponds to the restoration of ordering along the preferred chronoscalar gradient direction. In geometric terms, it is the re-establishment of alignment between the perturbed ordering vector and the local admissible axis of the manifold. This process is directly analogous to the recovery of isotropic support in an s-like atomic configuration after excitation. The relaxation timescale reflects how efficiently excess ordering can be redistributed through admissible corridors without violating finite-support or entropy-production constraints.

Transverse relaxation (T_2) probes a subtler property: the coherence of ordering *within* the admissible surface. Dephasing occurs when neighboring regions sample slightly different curvature, gradient magnitude, or coupling strength, causing ordering trajectories to diverge across the manifold. In chronoscalar terms, T_2 measures the stability of a yawed ordering sheet against differential curvature and microscopic anisotropy. Where atomic orbitals lock nodal geometry into fixed internal imaging, NMR coherence decays precisely because the manifold is being sampled dynamically rather than statically [18].

This comparison clarifies why NMR is exquisitely sensitive to environment. Chemical shift, dipolar coupling, and quadrupolar interactions are not arbitrary perturbations; they directly modify local curvature and admissibility structure. Changes in bonding, molecular motion, lattice symmetry, or strain alter the shape and stiffness of the ordering manifold, thereby reshaping relaxation pathways. Observed relaxation times encode how rapidly the chronoscalar field can reconfigure under these modified geometric constraints [19].

Crucially, NMR demonstrates that admissible ordering is not binary. There exists a continuous spectrum between fully stabilized internal imaging (as in atomic orbitals) and freely propagating transport (as in photons). NMR occupies the intermediate regime: ordering is coherent, localized, and structured, but not permanently locked. This is precisely the regime in which relaxation phenomena occur and where the chronoscalar manifold reveals its dynamic, non-stationary character.

From this perspective, the Bloch equations arise as a coarse-grained projection of manifold relaxation rather than as fundamental dynamical laws. They track the macroscopic components of ordering realignment without encoding the geometric admissibility conditions that govern it. Chronoscalar Field Theory supplies this missing structure, explaining why relaxation times are finite, why they depend on anisotropy and motion, and why coherence can be selectively preserved or destroyed under controlled perturbation [20].

The parallel with atomic orbitals is therefore structural rather than analogical. Both phenomena arise from the same underlying ordering field. Atomic orbitals demonstrate how curvature stabilizes imaging modes at high density and suppressed transport. NMR demonstrates how those

same ordering structures respond when coherence is displaced and must relax back through admissible pathways. Together, they establish that quantum structure and relaxation dynamics are complementary expressions of chronoscalar ordering under distinct boundary conditions, rather than separate domains governed by unrelated principles.

In the following section, this relaxation-based interpretation will be extended beyond laboratory spin systems to mesoscopic and macroscopic contexts, where partial ordering, anisotropic relaxation, and manifold yaw govern transport, alignment, and large-scale coherence.

9 NMR as Local Relocking: Chronoscalar Relaxation, Stiffness Scaling, and Predictive Rate Laws

Nuclear magnetic resonance is an unusually clean laboratory probe of *relocking dynamics*. Unlike orbital imaging (which diagnoses the static admissible manifold through bound-state geometry), NMR measures how a local ordering configuration returns to a stable corridor after being displaced. In standard physics this return is parameterized by the longitudinal and transverse relaxation times T_1 and T_2 [21,22]. In Chronoscalar Field Theory (CFT), these are not merely phenomenological constants: they are the observable response of the local chronoscalar ordering manifold to perturbation, governed by an admissibility-controlled stiffness and by curvature-induced anisotropy.

9.1 Observed Phenomenon and the Conventional Rate Structure

Experimentally, an ensemble of nuclear spins in a static field $\mathbf{B}_0$ exhibits (i) recovery of longitudinal magnetization M_z toward equilibrium with time constant T_1 and (ii) loss of transverse phase coherence $M_\perp$ with time constant T_2 [21,22,23]. In the standard Bloch–Redfield description, relaxation is driven by fluctuating local magnetic fields $\delta\mathbf{B}(t)$ produced by the environment [22,23,24]. Defining the nuclear Larmor frequency $\omega_0 = \gamma B_0$, one obtains the canonical spectral-density rate laws

$$\frac{1}{T_1} = \gamma^2 \left[S_{B_x B_x}(\omega_0) + S_{B_y B_y}(\omega_0) \right], \tag{1}$$

$$\frac{1}{T_2} = \frac{1}{2T_1} + \gamma^2 S_{B_z B_z}(0) + \left(\frac{1}{T_2} \right)_{\text{inh}}, \tag{2}$$

where $S_{AB}(\omega)$ denotes the (one-sided) power spectral density of fluctuations, and $(1/T_2)_{\text{inh}}$ collects static or quasi-static inhomogeneity (field gradients, susceptibility microstructure, unresolved couplings) [22,23]. These relations are stage-1 foundations: they are not in dispute, and they are precisely where a new theory must anchor itself to remain traceable.

The question CFT answers is: *what is the physical origin and scaling of $\delta\mathbf{B}(t)$ in a theory where ordering is primary?*

9.2 CFT Identification: The Relocking Coordinate and Its Chronoscalar Stiffness

In CFT a local "state" is not an ontological instant but a finite-support ordering configuration. For NMR the relevant configuration is a *local relocking coordinate* $\phi(t)$: a scalar phase-like variable describing how the spin environment is aligned with an admissible ordering corridor. This ϕ is not a quantum phase postulate; it is a coarse descriptor of how the local microenvironment (electrons, lattice, defects) is locked to the ordering manifold defined by $T(x^\mu)$.

The key point is that local perturbations displace ϕ from its admissible minimum, and the return to admissibility is a dissipative relaxation controlled by (i) a stiffness K and (ii) a damping

Γ. The minimal admissible dynamics consistent with finite support and positive entropy production is an overdamped relocking equation

$$\Gamma\dot{\phi}(t) + K\,\phi(t) = \xi(t), \tag{3}$$

where $\xi(t)$ is a stationary noise term representing microscopic fluctuations that are *allowed* by admissibility. The noise is constrained by a fluctuation–dissipation relation at temperature Θ [25,26]:

$$\langle \xi(t)\xi(0)\rangle = 2\Gamma k_B\Theta\,\delta(t), \tag{4}$$

which ensures the system relaxes to a stationary distribution rather than an inadmissible instant.

Equation (37) is the mathematical statement of "local relocking" in CFT: K encodes the ordering cost of misalignment (stiffness of the local admissible manifold), and Γ encodes irreversible dissipation into admissible channels.

9.3 From Relocking to Measured NMR: Explicit Spectral Densities

The nuclear spin does not couple to ϕ directly; it couples to the *effective* local magnetic field produced by its environment. The minimal traceable coupling is linear in the relocking coordinate for small displacements:

$$\delta B_\alpha(t) = a_\alpha\,\phi(t), \qquad \alpha \in \{x, y, z\}. \tag{5}$$

The coefficients a_α encode hyperfine and dipolar pathways (the stage-1 mechanisms) [**?**, **?**] but in CFT their *statistical drive* is governed by the relocking dynamics of ϕ.

Solving (37) in Fourier space gives

$$\phi(\omega) = \frac{\xi(\omega)}{K + i\omega\Gamma}. \tag{6}$$

Using (38), the spectral density of ϕ is

$$S_{\phi\phi}(\omega) = \frac{2\Gamma k_B\Theta}{K^2 + (\omega\Gamma)^2}. \tag{7}$$

Then (39) implies

$$S_{B_\alpha B_\alpha}(\omega) = a_\alpha^2\,S_{\phi\phi}(\omega). \tag{8}$$

Substituting into (35)–(36), one obtains the explicit predictive rate laws:

$$\frac{1}{T_1} = \gamma^2(a_x^2 + a_y^2)\,\frac{2\Gamma k_B\Theta}{K^2 + (\omega_0\Gamma)^2}, \tag{9}$$

$$\frac{1}{T_2} = \frac{1}{2T_1} + \gamma^2 a_z^2\,\frac{2\Gamma k_B\Theta}{K^2} + \left(\frac{1}{T_2}\right)_{\text{inh}}. \tag{10}$$

Equations (43)–(44) are the central mathematical prediction: *NMR relaxation is set by the stiffness K of local chronoscalar relocking and its damping Γ, not by a free phenomenological clock.*

9.4 Predicted Regimes and the Shape of the Graphs

The observed heavy-atom pattern (very long T_1 but very fragile/short T_2 in many environments) follows from a two-term competition that is explicit in (44). The theory predicts distinct regimes:

Stiff-manifold regime ($K \gg \omega_0\Gamma$). Here the spectral density at ω_0 is suppressed as $S_{\phi\phi}(\omega_0) \sim 2\Gamma k_B\Theta/K^2$, giving

$$T_1 \sim \frac{K^2}{2\gamma^2(a_x^2 + a_y^2)\Gamma k_B\Theta}. \tag{11}$$

Thus, increasing stiffness K drives T_1 upward *quadratically*. This is precisely the trend expected when moving from light atoms (weak curvature support) to heavy, concurrency-dominated atoms (strong curvature support).

Transverse coherence and curvature microstructure. In contrast, T_2 has two distinct contributions: (i) a dynamic relocking term that is *also* suppressed by stiffness ($\propto 1/K^2$) and (ii) an inhomogeneous term $(1/T_2)_{\text{inh}}$ that *grows* with curvature anisotropy and manifold rank reduction [22,23].

CFT makes this explicit by tying inhomogeneity to spatial variation of the chronoscalar Hessian $H_{ij} = \nabla_i\nabla_j T$. The simplest traceable model is

$$\left(\frac{1}{T_2}\right)_{\text{inh}} \equiv \Delta\omega_{\text{rms}} \quad \propto \quad \gamma\,\chi_{\text{eff}}\,\sqrt{\text{Var}[\mathcal{I}(H)]}, \tag{12}$$

where $\mathcal{I}(H)$ is a scalar invariant (or small set of invariants) of the local Hessian (e.g. $\text{tr}\,H$, $\det H$, or an anisotropy measure built from eigenvalue differences), and χ_{eff} is an effective coupling converting admissibility curvature variations into field offsets through the electronic environment. The key prediction is that heavy atoms and anisotropic manifolds increase $\text{Var}[\mathcal{I}(H)]$, producing short T_2 even while T_1 remains long.

Therefore, the *graph form* expected in stiff-manifold materials is:

$$T_1 \propto K^2 \quad \text{(growth with atomic stiffness)}, \tag{13}$$

$$T_2 \approx \left[\gamma\,\chi_{\text{eff}}\,\sqrt{\text{Var}[\mathcal{I}(H)]}\right]^{-1} \quad \text{(collapse with curvature microstructure)}. \tag{14}$$

This is not a qualitative story; it is the explicit mathematical reason the two curves can move in opposite directions.

9.5 Connecting Stiffness K to Atomic "Strength": A Shell-Concurrency Scaling Law

To connect the above rate laws to atomic identity, CFT requires an estimate of how K scales with shell concurrency and baryonic stiffening. The chronoscalar equation of motion already contains the stiffening factor $(1 + \kappa\rho_b)$. A minimal stiffness functional consistent with the action is

$$K \;\equiv\; \int_{\mathcal{V}} d^3x\,(1 + \kappa\rho_b)\,|\nabla T|^2\,W(x), \tag{15}$$

where $W(x)$ is a localization weight selecting the ordering volume relevant to the nuclear environment.

The key atomic input is that in heavy atoms the relevant ordering volume is dominated not by a single shell but by concurrent shells. Denote by N_{conc} the effective number of concurrently overlapping shells contributing to curvature in the same ordering volume. Then the simplest concurrency scaling is

$$K \sim K_0\,(1 + \kappa\rho_b)\,N_{\text{conc}}^2, \tag{16}$$

where the square reflects the fact that curvature support is produced by interacting (not merely additive) shell components: concurrent anisotropy produces yaw and rank reduction, which is a second-order geometric effect.

Substituting (50) into (45) yields an explicit predicted scaling trend:

$$T_1 \propto (1 + \kappa\rho_b)^2 \, N_{\text{conc}}^4. \tag{17}$$

This is the concrete mathematical reason heavy, concurrency-rich atoms exhibit orders-of-magnitude increases in T_1: the effect is steep in concurrency, not linear.

The corresponding transverse behavior follows (46): increasing concurrency increases yawed anisotropy and therefore increases curvature-variance invariants, shrinking T_2 in many real materials.

9.6 Conceptual Closure: Orbitals versus NMR as Static versus Dynamic Manifold Diagnostics

The orbital hierarchy discussed in the preceding section diagnoses the *static* admissible ordering manifold through stabilized internal imaging modes. In contrast, NMR probes the *dynamic* behavior of that same manifold by measuring how a locally perturbed ordering configuration returns to admissibility through longitudinal and transverse relocking. These are not separate structures or unrelated physical mechanisms. They are two distinct experimental projections of the same underlying ordering geometry.

In the static limit, shell concurrency and anisotropic yaw determine the rank, orientation, and internal imaging structure of the admissible manifold, giving rise to the familiar orbital configurations observed in atomic spectroscopy. In the dynamic limit sampled by NMR, the same concurrency and yaw control the stiffness K of the ordering corridor and the variance of curvature invariants constructed from the transverse Hessian. These quantities directly govern the observed relaxation times T_1 and T_2, as well as their strong orientation dependence in real materials.

What appears in one context as nodal structure and angular imaging appears in the other as linewidth broadening, dephasing, and relaxation anisotropy. NMR therefore provides an independent laboratory axis for measuring the same admissible ordering manifold inferred from orbital structure and Fourier-space collapse. Taken together, static orbital imaging and dynamic NMR relaxation complete the atomic-to-relaxation link required for a unified chronoscalar account, demonstrating that geometric structure and dynamical response are inseparable manifestations of a single admissible manifold.

9.7 Conceptual Closure: Orbitals versus NMR as Static versus Dynamic Manifold Diagnostics

The orbital hierarchy discussed in the preceding section diagnoses the *static* admissible ordering manifold through stabilized internal imaging modes. In contrast, NMR probes the *dynamic* behavior of that same manifold by measuring how a locally perturbed ordering configuration returns to admissibility through longitudinal and transverse relocking. These are not separate structures or unrelated physical mechanisms. They are two distinct experimental projections of the same underlying ordering geometry.

In the static limit, shell concurrency and anisotropic yaw determine the rank, orientation, and internal imaging structure of the admissible manifold, giving rise to the familiar s-, p-, and d-like orbital configurations. In the dynamic limit sampled by NMR, the same concurrency and yaw control the stiffness K of the ordering corridor and the variance of curvature invariants built from

the transverse Hessian, which in turn govern the observed relaxation times T_1 and T_2. What appears in one context as nodal structure and angular imaging appears in the other as orientation-dependent linewidths, dephasing, and relaxation anisotropy.

NMR therefore provides an independent and complementary laboratory axis for measuring the same admissible ordering manifold that is inferred from orbital structure and Fourier-space collapse. Taken together, static orbital imaging and dynamic NMR relaxation complete the atomic-to-relaxation link required for a unified chronoscalar description of microscopic ordering, demonstrating that geometric structure and dynamical response are inseparable manifestations of a single admissible manifold.

10 NMR as Local Relocking: Chronoscalar Relaxation, Stiffness Scaling, and Predictive Rate Laws

Nuclear magnetic resonance is an unusually clean laboratory probe of *relocking dynamics*. Unlike orbital imaging (which diagnoses the static admissible manifold through bound-state geometry), NMR measures how a local ordering configuration returns to a stable corridor after being displaced. In standard physics this return is parameterized by the longitudinal and transverse relaxation times T_1 and T_2 [21,22]. In Chronoscalar Field Theory (CFT), these are not merely phenomenological constants: they are the observable response of the local chronoscalar ordering manifold to perturbation, governed by an admissibility-controlled stiffness and by curvature-induced anisotropy.

10.1 Observed Phenomenon and the Conventional Rate Structure

Experimentally, an ensemble of nuclear spins in a static field $\mathbf{B}_0$ exhibits (i) recovery of longitudinal magnetization M_z toward equilibrium with time constant T_1 and (ii) loss of transverse phase coherence $M_\perp$ with time constant T_2 [21–23]. In the standard Bloch–Redfield description, relaxation is driven by fluctuating local magnetic fields $\delta\mathbf{B}(t)$ produced by the environment [22–24]. Defining the nuclear Larmor frequency $\omega_0 = \gamma B_0$, one obtains the canonical spectral-density rate laws

$$\frac{1}{T_1} = \gamma^2 \left[S_{B_x B_x}(\omega_0) + S_{B_y B_y}(\omega_0) \right], \tag{18}$$

$$\frac{1}{T_2} = \frac{1}{2T_1} + \gamma^2 S_{B_z B_z}(0) + \left(\frac{1}{T_2} \right)_{\text{inh}}, \tag{19}$$

where $S_{AB}(\omega)$ denotes the (one-sided) power spectral density of fluctuations, and $(1/T_2)_{\text{inh}}$ collects static or quasi-static inhomogeneity (field gradients, susceptibility microstructure, unresolved couplings) [22,23]. These relations are the foundations: they are not in dispute, and they are precisely where a new theory must anchor itself to remain traceable.

The question CFT answers is: *what is the physical origin and scaling of $\delta\mathbf{B}(t)$ in a theory where ordering is primary?*

10.2 CFT Identification: The Relocking Coordinate and Its Chronoscalar Stiffness

In CFT a local "state" is not an ontological instant but a finite-support ordering configuration. For NMR the relevant configuration is a *local relocking coordinate* $\phi(t)$: a scalar phase-like variable describing how the spin environment is aligned with an admissible ordering corridor. This ϕ is not a quantum phase postulate; it is a coarse descriptor of how the local microenvironment (electrons, lattice, defects) is locked to the ordering manifold defined by $T(x^\mu)$.

The key point is that local perturbations displace ϕ from its admissible minimum, and the return to admissibility is a dissipative relaxation controlled by (i) a stiffness K and (ii) a damping Γ. The minimal admissible dynamics consistent with finite support and positive entropy production is an overdamped relocking equation

$$\Gamma\dot{\phi}(t) + K\,\phi(t) = \xi(t), \tag{20}$$

where $\xi(t)$ is a stationary noise term representing microscopic fluctuations that are *allowed* by admissibility. The noise is constrained by a fluctuation–dissipation relation at temperature Θ [25,26]:

$$\langle \xi(t)\xi(0)\rangle = 2\Gamma k_B\Theta\,\delta(t), \tag{21}$$

which ensures the system relaxes to a stationary distribution rather than an inadmissible instant.

Equation (37) is the mathematical statement of "local relocking" in CFT: K encodes the ordering cost of misalignment (stiffness of the local admissible manifold), and Γ encodes irreversible dissipation into admissible channels.

10.3 From Relocking to Measured NMR: Explicit Spectral Densities

The nuclear spin does not couple to ϕ directly; it couples to the *effective* local magnetic field produced by its environment. The minimal traceable coupling is linear in the relocking coordinate for small displacements:

$$\delta B_\alpha(t) = a_\alpha\,\phi(t), \qquad \alpha \in \{x, y, z\}. \tag{22}$$

The coefficients a_α encode hyperfine and dipolar pathways (the stage-1 mechanisms) [22,23], but in CFT their *statistical drive* is governed by the relocking dynamics of ϕ.

Solving (37) in Fourier space gives

$$\phi(\omega) = \frac{\xi(\omega)}{K + i\omega\Gamma}. \tag{23}$$

Using (38), the spectral density of ϕ is

$$S_{\phi\phi}(\omega) = \frac{2\Gamma k_B\Theta}{K^2 + (\omega\Gamma)^2}. \tag{24}$$

Then (39) implies

$$S_{B_\alpha B_\alpha}(\omega) = a_\alpha^2\,S_{\phi\phi}(\omega). \tag{25}$$

Substituting into (35)–(36), one obtains the explicit predictive rate laws:

$$\frac{1}{T_1} = \gamma^2(a_x^2 + a_y^2)\,\frac{2\Gamma k_B\Theta}{K^2 + (\omega_0\Gamma)^2}, \tag{26}$$

$$\frac{1}{T_2} = \frac{1}{2T_1} + \gamma^2 a_z^2\,\frac{2\Gamma k_B\Theta}{K^2} + \left(\frac{1}{T_2}\right)_{\text{inh}}. \tag{27}$$

Equations (43)–(44) are the central mathematical prediction: *NMR relaxation is set by the stiffness K of local chronoscalar relocking and its damping Γ, not by a free phenomenological clock.*

10.4 Predicted Regimes and the Shape of the Graphs

The observed heavy-atom pattern (very long T_1 but very fragile/short T_2 in many environments) follows from a two-term competition that is explicit in (44). The theory predicts distinct regimes:

Stiff-manifold regime ($K \gg \omega_0\Gamma$). Here the spectral density at ω_0 is suppressed as $S_{\phi\phi}(\omega_0) \sim 2\Gamma k_B\Theta/K^2$, giving

$$T_1 \sim \frac{K^2}{2\gamma^2(a_x^2 + a_y^2)\Gamma k_B\Theta}. \tag{28}$$

Thus, increasing stiffness K drives T_1 upward *quadratically*. This is precisely the trend expected when moving from light atoms (weak curvature support) to heavy, concurrency-dominated atoms (strong curvature support).

Transverse coherence and curvature microstructure. In contrast, T_2 has two distinct contributions: (i) a dynamic relocking term that is *also* suppressed by stiffness ($\propto 1/K^2$) and (ii) an inhomogeneous term $(1/T_2)_{\text{inh}}$ that *grows* with curvature anisotropy and manifold rank reduction [22,23].

CFT makes this explicit by tying inhomogeneity to spatial variation of the chronoscalar Hessian $H_{ij} = \nabla_i\nabla_j T$. The simplest traceable model is

$$\left(\frac{1}{T_2}\right)_{\text{inh}} \equiv \Delta\omega_{\text{rms}} \quad \propto \quad \gamma\,\chi_{\text{eff}}\,\sqrt{\text{Var}[\mathcal{I}(H)]}, \tag{29}$$

where $\mathcal{I}(H)$ is a scalar invariant (or small set of invariants) of the local Hessian (e.g. $\text{tr}\,H$, $\det H$, or an anisotropy measure built from eigenvalue differences), and χ_{eff} is an effective coupling converting admissibility curvature variations into field offsets through the electronic environment.

Therefore, the *graph form* expected in stiff-manifold materials is:

$$T_1 \propto K^2 \quad \text{(growth with atomic stiffness)}, \tag{30}$$

$$T_2 \approx \left[\gamma\,\chi_{\text{eff}}\,\sqrt{\text{Var}[\mathcal{I}(H)]}\right]^{-1} \quad \text{(collapse with curvature microstructure)}. \tag{31}$$

This is not a qualitative story; it is the explicit mathematical reason the two curves can move in opposite directions.

10.5 Connecting Stiffness K to Atomic "Strength": A Shell-Concurrency Scaling Law

To connect the above rate laws to atomic identity, CFT requires an estimate of how K scales with shell concurrency and baryonic stiffening. The chronoscalar equation of motion already contains the stiffening factor $(1 + \kappa\rho_b)$. A minimal stiffness functional consistent with the action is

$$K \;\equiv\; \int_{\mathcal{V}} d^3x\,(1 + \kappa\rho_b)\,|\nabla T|^2\,W(x), \tag{32}$$

where $W(x)$ is a localization weight selecting the ordering volume relevant to the nuclear environment.

The key atomic input is that in heavy atoms the relevant ordering volume is dominated not by a single shell but by concurrent shells. Denote by N_{conc} the effective number of concurrently overlapping shells contributing to curvature in the same ordering volume. Then the simplest concurrency scaling is

$$K \sim K_0\,(1 + \kappa\rho_b)\,N_{\text{conc}}^2, \tag{33}$$

where the square reflects the fact that curvature support is produced by interacting (not merely additive) shell components: concurrent anisotropy produces yaw and rank reduction, which is a second-order geometric effect.

Substituting (50) into (45) yields an explicit predicted scaling trend:

$$T_1 \propto (1 + \kappa\rho_b)^2 \, N_{\text{conc}}^4. \tag{34}$$

10.6 Conceptual Closure: Orbitals versus NMR as Static versus Dynamic Manifold Diagnostics

The orbital hierarchy (previous section) diagnoses the *static* admissible manifold through stabilized imaging modes. NMR diagnoses the *dynamic* return to admissibility through relocking response. The same underlying objects appear in both:

- Shell concurrency and anisotropic yaw set the manifold rank and imaging structure (orbitals).
- The same concurrency and yaw set the stiffness K and curvature-variance invariants governing T_1 and T_2 (NMR).

Thus, NMR provides an independent laboratory axis for measuring the same ordering manifold inferred from orbital structure and Fourier collapse, completing the atomic-to-relaxation link required for a unified chronoscalar account.

11 NMR as Local Relocking: Chronoscalar Relaxation, Stiffness Scaling, and Predictive Rate Laws

Nuclear magnetic resonance is an unusually clean laboratory probe of *relocking dynamics*. Unlike orbital imaging, which diagnoses the static admissible manifold through stabilized internal imaging modes, NMR measures how a local ordering configuration returns to an admissible corridor after being displaced. In conventional physics this return is parameterized by the longitudinal and transverse relaxation times T_1 and T_2, with the phenomenology organized by the Bloch equations and their microscopic refinements [27,28]. In Chronoscalar Field Theory (CFT), these times are not fitted constants: they are the observable response of the local chronoscalar ordering manifold to perturbation, governed by an admissibility-controlled stiffness and by curvature-induced anisotropy.

11.1 Observed Phenomenon and the Conventional Rate Structure

Experimentally, an ensemble of nuclear spins in a static field $\mathbf{B}_0$ exhibits (i) recovery of longitudinal magnetization M_z toward equilibrium with time constant T_1 and (ii) loss of transverse phase coherence $M_\perp$ with time constant T_2. In the Bloch–Redfield description, relaxation is driven by fluctuating local magnetic fields $\delta\mathbf{B}(t)$ produced by the environment. Defining the nuclear Larmor frequency $\omega_0 = \gamma B_0$, one obtains the canonical spectral-density rate laws

$$\frac{1}{T_1} = \gamma^2 \left[S_{B_x B_x}(\omega_0) + S_{B_y B_y}(\omega_0) \right], \tag{35}$$

$$\frac{1}{T_2} = \frac{1}{2T_1} + \gamma^2 S_{B_z B_z}(0) + \left(\frac{1}{T_2} \right)_{\text{inh}}, \tag{36}$$

where $S_{AB}(\omega)$ denotes the one-sided power spectral density of fluctuations and $(1/T_2)_{\text{inh}}$ collects static or quasi-static inhomogeneity (field gradients, susceptibility microstructure, unresolved couplings). These relations constitute the accepted foundation of NMR theory and provide the reference point that any deeper theory must reproduce [27–30].

The question addressed by CFT is therefore not whether Eqs. (35)–(36) hold, but *what physical object determines the magnitude and scaling of the spectral densities* in systems where ordering, rather than noise, is primary.

11.2 CFT Identification: The Relocking Coordinate and Chronoscalar Stiffness

In CFT a local "state" is not an ontological instant but a finite-support ordering configuration. For NMR the relevant configuration is a *local relocking coordinate* $\phi(t)$: a scalar phase-like variable describing how the spin environment is aligned with an admissible ordering corridor of the chronoscalar field $T(x^\mu)$. This variable is not a postulated quantum phase; it is a coarse descriptor of how the electronic and lattice environment remains locked to the local ordering manifold.

Perturbations displace ϕ from its admissible minimum. The return to admissibility is dissipative and governed by a stiffness K and a damping coefficient Γ. The minimal admissible dynamics consistent with finite support and positive entropy production is an overdamped relocking equation,

$$\Gamma\dot{\phi}(t) + K\,\phi(t) = \xi(t), \tag{37}$$

where $\xi(t)$ represents microscopic fluctuations that are permitted by admissibility. Thermodynamic consistency requires a fluctuation–dissipation relation,

$$\langle \xi(t)\xi(0)\rangle = 2\Gamma k_B\Theta\,\delta(t), \tag{38}$$

which is the same structural requirement that underlies standard stochastic derivations of Redfield and Bloembergen–Purcell–Pound (BPP) relaxation theory [28,31]. . Equation (37) is the mathematical statement of local relocking in CFT: K encodes the ordering cost of misalignment (stiffness of the admissible manifold), while Γ encodes irreversible dissipation into admissible channels.

11.3 From Relocking to Measured NMR: Explicit Spectral Densities

The nuclear spin couples not to ϕ directly, but to the effective local magnetic field generated by its environment. To leading order the coupling is linear,

$$\delta B_\alpha(t) = a_\alpha\,\phi(t), \qquad \alpha \in \{x, y, z\}, \tag{39}$$

where a_α encodes hyperfine and dipolar pathways (stage-1 physics). The statistical properties of $\delta\mathbf{B}(t)$ are therefore controlled by the relocking dynamics of ϕ.

Solving Eq. (37) in Fourier space yields

$$\phi(\omega) = \frac{\xi(\omega)}{K + i\omega\Gamma}, \tag{40}$$

and hence the spectral density

$$S_{\phi\phi}(\omega) = \frac{2\Gamma k_B\Theta}{K^2 + (\omega\Gamma)^2}. \tag{41}$$

Using Eq. (39), one finds

$$S_{B_\alpha B_\alpha}(\omega) = a_\alpha^2\,S_{\phi\phi}(\omega). \tag{42}$$

Substitution into Eqs. (35)–(36) yields the CFT rate laws

$$\frac{1}{T_1} = \gamma^2(a_x^2 + a_y^2)\,\frac{2\Gamma k_B\Theta}{K^2 + (\omega_0\Gamma)^2}, \tag{43}$$

$$\frac{1}{T_2} = \frac{1}{2T_1} + \gamma^2 a_z^2\,\frac{2\Gamma k_B\Theta}{K^2} + \left(\frac{1}{T_2}\right)_{\text{inh}}. \tag{44}$$

These expressions are fit-ready and reduce to standard forms when K is treated as an empirical parameter. In CFT, however, K is a geometric property of the ordering manifold. As shown in Figure 3, the high-magnification view of the local admissible ordering manifold illustrates how the nuclear spin precesses in the external field $\mathbf{B}_0$ while the surrounding electronic and lattice environment induces anisotropic curvature.

11.4 Predicted Regimes and Graph Shapes

In the stiff-manifold regime $K \gg \omega_0 \Gamma$, the spectral density at the Larmor frequency is suppressed,

$$S_{\phi\phi}(\omega_0) \approx \frac{2\Gamma k_B \Theta}{K^2},$$

leading to

$$T_1 \sim \frac{K^2}{2\gamma^2 (a_x^2 + a_y^2) \Gamma k_B \Theta}. \tag{45}$$

Thus T_1 grows quadratically with stiffness.

Transverse coherence behaves differently. Static and quasi-static curvature anisotropy produces a contribution

$$\left(\frac{1}{T_2}\right)_{\text{inh}} \equiv \Delta\omega_{\text{rms}} \;\propto\; \gamma\, \chi_{\text{eff}} \sqrt{\text{Var}[\mathcal{I}(H)]}, \tag{46}$$

where $H_{ij} = \nabla_i \nabla_j T$ is the chronoscalar Hessian and $\mathcal{I}(H)$ is an invariant characterizing anisotropy. Consequently,

$$T_1 \propto K^2, \tag{47}$$

$$T_2 \approx \left[\gamma\, \chi_{\text{eff}} \sqrt{\text{Var}[\mathcal{I}(H)]}\right]^{-1} \quad \text{when inhomogeneity dominates.} \tag{48}$$

11.5 Physical Example: ^{29}Si in Single-Crystal Silicon

A well-documented example is enriched ^{29}Si in single-crystal silicon at room temperature and fields near 7 T. Experiments report longitudinal relaxation times $T_1 \approx$ 2–3 hours, strong orientation-dependent linewidths, and splittings up to ~ 1.2 kHz depending on crystal axis [32].

For ^{29}Si at 7 T the Larmor frequency is $f \approx 59.6$ MHz, giving

$$\omega_0 \approx 3.74 \times 10^8\, \text{s}^{-1}.$$

Observed linewidths $\Delta f \sim 10^3$ Hz correspond to

$$\Delta\omega_{\text{rms}} \sim \pi \Delta f \sim 3 \times 10^3\, \text{s}^{-1},$$

implying millisecond-scale dephasing while T_1 remains hours-scale. This simultaneous occurrence of extreme longitudinal stiffness and fragile transverse coherence is exactly the regime predicted by Eqs. (45) and (46) when the admissible manifold is stiff but anisotropic [32].

11.6 Atomic Strength and Concurrency Scaling

In CFT the stiffness K is determined by shell concurrency and baryonic stiffening. A minimal functional consistent with the action is

$$K = \int_{\mathcal{V}} d^3x\, (1 + \kappa\rho_b)\, |\nabla T|^2\, W(x), \tag{49}$$

where $W(x)$ localizes the nuclear environment. If N_{conc} shells contribute concurrently, the leading scaling is

$$K \sim K_0\, (1 + \kappa\rho_b)\, N_{\text{conc}}^2. \tag{50}$$

Substitution into Eq. (45) yields

$$T_1 \propto (1 + \kappa\rho_b)^2\, N_{\text{conc}}^4. \tag{51}$$

This steep dependence explains why modest increases in shell concurrency produce orders-of-magnitude changes in T_1 across different atomic environments.

11.7 Closure

Atomic orbitals diagnose the *static* admissible geometry of the chronoscalar manifold. NMR diagnoses the *dynamic* return to admissibility after perturbation. The same geometric objects—shell concurrency, curvature anisotropy, and stiffness—govern both. NMR therefore provides an independent, quantitative laboratory measurement of the ordering manifold inferred from orbital structure, completing the atomic-to-relaxation link required for a unified chronoscalar account.

12 ESR and Electronic Phase Relocking: Spin–Orbit Geometry, Berry Accumulation, and Chronoscalar Stiffness

Electron spin resonance (ESR), together with its modern solid-state realizations (EPR, spin-resolved ARPES, and Berry-phase measurements), provides the electronic analog of the NMR relocking phenomena discussed in the previous section. Where NMR probes the return of *nuclear* ordering to admissible corridors through lattice- and electron-mediated curvature, ESR probes the relocking of *electronic* degrees of freedom themselves. The distinction is crucial: ESR is sensitive not merely to static shell geometry, but to how electronic phase and spin orientation re-lock to the same admissible ordering manifold inferred earlier from orbital structure and Fourier collapse.

In standard physics, ESR is treated as a resonance phenomenon driven by Zeeman splitting and spin–orbit coupling, with relaxation governed by phenomenological rates and microscopic scattering models. The foundational framework is well established and experimentally verified. [33–35] Chronoscalar Field Theory (CFT) does not dispute this foundation. Instead, it identifies the *geometric origin* of those rates and phase responses as manifestations of the same admissible ordering manifold that governs orbital structure and nuclear relaxation.

12.1 Observed ESR Phenomenology and Anchors

Electron spin resonance probes the response of electronic spins to a static magnetic field $\mathbf{B}_0$ through resonant absorption of electromagnetic radiation. The basic resonance condition is

$$\hbar\omega_0 = g\mu_B B_0, \tag{52}$$

where g is the effective Landé factor and μ_B is the Bohr magneton. In real solids, the ESR signal is never characterized solely by the resonance frequency: linewidths, g-tensor anisotropies, and the electronic relaxation times T_{1e} and T_{2e} carry the dominant physical information. These quantities are observed to depend strongly on crystal orientation, local symmetry, spin–orbit coupling strength, and the detailed electronic environment. A large body of experimental literature, beginning with classic studies of transition-metal ions and extending to heavy-element and surface-state systems, documents these dependencies in a systematic and reproducible way [33,34].

Two empirical features of ESR are particularly important when interpreted through the chronoscalar framework. First, ESR linewidths and g-tensor components commonly exhibit pronounced orientation dependence even in chemically and structurally homogeneous materials. Rotating a single crystal in a fixed field can change the linewidth by orders of magnitude, indicating that the dominant broadening mechanism is geometric rather than statistical in origin. This behavior is well established in systems where crystal-field splitting and spin–orbit coupling generate strongly anisotropic local environments, and it persists even when motional averaging or exchange narrowing would otherwise be expected to suppress inhomogeneity [35].

Second, in heavy elements and in systems with strong spin–orbit interaction, electronic phase coherence is observed to be remarkably fragile despite the presence of sharply defined static orbital

structure. Angle-resolved photoemission and surface-sensitive ESR studies show that well-resolved bands and orbitals can coexist with broad ESR lines and rapid transverse dephasing, indicating that the mechanisms controlling static electronic structure are not the same as those governing dynamical phase stability [36]. This mirrors, at the electronic level, the pattern already identified in NMR, where systems may exhibit very long longitudinal relaxation times while simultaneously displaying rapid loss of phase coherence and strong linewidth broadening.

Within CFT, these empirical facts are not treated as anomalies or material-specific pathologies. Instead, they serve as stage-1 anchors that any deeper ordering theory must reproduce. ESR directly samples how electronic phases relock within an anisotropic, curvature-bearing ordering manifold, making it intrinsically more sensitive to transverse microstructure, yaw, and rank reduction than to the absolute stiffness that controls longitudinal energy exchange. The observed orientation dependence and coherence fragility are therefore not secondary effects, but primary diagnostics of the transverse admissible structure that ESR is uniquely positioned to reveal [33–36].

12.2 CFT Identification: Electronic Relocking Coordinate

In Chronoscalar Field Theory, electronic states are not instantaneous eigenvectors but finite-support ordering configurations embedded in the chronoscalar manifold. The electronic analog of the nuclear relocking coordinate is an *electronic phase–spin relocking variable*, denoted $\theta(t)$, which encodes the alignment of the electronic spin-orbital texture with the local admissible ordering corridor.

As with NMR, perturbations displace θ from its admissible minimum, and relaxation proceeds dissipatively:

$$\Gamma_e \dot{\theta}(t) + K_e\, \theta(t) = \eta(t), \tag{53}$$

where K_e is the electronic ordering stiffness and Γ_e is the electronic dissipation coefficient. The noise term $\eta(t)$ obeys a fluctuation–dissipation relation identical in form to the nuclear case, ensuring positive entropy production and finite support. [34,37]

The crucial distinction is that K_e is controlled primarily by *spin–orbit curvature* and shell concurrency rather than by nuclear dipolar geometry. This immediately explains why ESR is exquisitely sensitive to anisotropy in heavy elements.

12.3 Spin–Orbit Coupling as Curvature Locking

In conventional theory, spin–orbit coupling is introduced as a relativistic correction proportional to $\mathbf{L} \cdot \mathbf{S}$. In CFT, the same term appears as a geometric locking between electronic transport modes and the anisotropic Hessian of the chronoscalar field. Regions of strong curvature anisotropy enforce preferred orientations of electronic spin textures, producing effective g-tensor anisotropy and orientation-dependent resonance conditions.

This interpretation aligns directly with experimental ESR observations in tungsten, platinum, and gold surfaces, where spin splitting and anisotropic linewidths correlate with surface orientation and band curvature rather than with simple atomic parameters [36,38].

12.4 Berry Phase as Ordering Holonomy

A defining feature of modern electronic spectroscopy is the observation of Berry phases accumulated along closed trajectories in momentum or parameter space. In CFT, Berry phase is not an abstract geometric phase of a Hilbert space; it is the integrated holonomy of the chronoscalar ordering

manifold sampled by electronic transport or relocking:

$$\gamma_{\text{Berry}} = \oint \mathcal{A}_i \, dk_i \quad \longleftrightarrow \quad \oint n^\mu \nabla_\mu T \, ds. \tag{54}$$

Here, the phase arises because electronic states traverse regions of differing curvature and admissibility. This interpretation naturally unifies ESR phase shifts, spin-momentum locking, and Berry curvature observed in topological materials [39,40].

Importantly, Berry phase accumulation is slow compared to electronic hopping but fast compared to nuclear relocking, placing it squarely between the ESR and NMR regimes—exactly where CFT predicts the chronoscalar manifold should be dynamically sampled.

12.5 Predicted ESR Rate Laws and Anisotropy

Proceeding as in the NMR case, the effective fluctuating fields experienced by electronic spins arise from $\theta(t)$:

$$\delta B_\alpha^{(e)}(t) = b_\alpha \, \theta(t), \tag{55}$$

leading to spectral densities

$$S_{\alpha\alpha}^{(e)}(\omega) = b_\alpha^2 \frac{2\Gamma_e k_B \Theta}{K_e^2 + (\omega \Gamma_e)^2}. \tag{56}$$

The resulting relaxation rates satisfy

$$\frac{1}{T_{1e}} \propto \frac{\Gamma_e}{K_e^2 + (\omega_0 \Gamma_e)^2}, \tag{57}$$

$$\frac{1}{T_{2e}} \approx \frac{1}{2T_{1e}} + \Delta\omega_{\text{aniso}}, \tag{58}$$

where $\Delta\omega_{\text{aniso}}$ is controlled by curvature-induced g-tensor and spin–orbit anisotropy. This reproduces the empirically observed dominance of anisotropic dephasing in heavy-element ESR [33,35].

12.6 Conceptual Closure: ESR as the Electronic Relocking Analog of NMR

Within Chronoscalar Field Theory, electron spin resonance (ESR) and nuclear magnetic resonance (NMR) emerge not as distinct physical mechanisms but as complementary probes of a single admissible ordering manifold sampled at different mass, coupling, and stiffness scales. The distinction between the two is therefore not ontological but kinematic: each interrogates how a displaced degree of freedom relocks to the same underlying chronoscalar geometry under different admissibility costs.

Atomic orbital structure provides the static baseline. Orbital imaging and spectroscopy diagnose the frozen admissible geometry itself, revealing how electronic probability density is confined by the curvature and anisotropy of the ordering manifold. These static observables establish the shape, rank reduction, and concurrency of the manifold but do not probe its dynamic response.

ESR probes the next layer: electronic phase relocking. When an electronic spin is displaced from its admissible orientation, its return to equilibrium reflects the stiffness and holonomy of the manifold at electronic length and time scales. Because electrons couple strongly to lattice anisotropy, spin–orbit interaction, and surface curvature, ESR is particularly sensitive to transverse manifold structure and geometric phase accumulation. Orientation-dependent g-factors, anisotropic linewidths, and Berry-phase-like shifts observed in ESR experiments directly encode curvature-induced phase winding and holonomy of the admissible corridor [33–39].

NMR, by contrast, probes nuclear relocking mediated through the same manifold but filtered by the electronic environment. Nuclear spins couple weakly and indirectly to curvature via hyperfine, dipolar, and chemical-shift pathways, producing dramatically longer longitudinal relaxation times while remaining exquisitely sensitive to spatial variations of the local Hessian. As developed in the preceding sections, this separation explains how systems may exhibit extremely long T_1 while simultaneously showing rapid transverse dephasing and orientation-dependent linewidth broadening [27–32].

The resulting hierarchy of timescales—electronic phase relocking (ESR), nuclear phase relocking (NMR), and macroscopic transport or relaxation—does not imply multiple underlying physical principles. Instead, it reflects different projections of the same admissible ordering structure onto degrees of freedom with different inertia, coupling strength, and entropy production cost. ESR samples the fast, curvature-sensitive electronic sector of the manifold; NMR samples the slow, stiffness-dominated nuclear sector; and macroscopic observables integrate both into effective transport and relaxation laws.

This unification provides a concrete predictive advantage. Any material or geometry that produces strong anisotropy or holonomy in ESR must, within CFT, also produce corresponding signatures in NMR—specifically, suppressed T_2, enhanced orientation dependence, and decoupling between T_1 and T_2—even when conventional mechanisms would predict otherwise. Conversely, systems exhibiting anomalously long nuclear coherence imply unusually stiff electronic corridors, constraining the allowable orbital and ESR response. In this sense, ESR and NMR together form a closed diagnostic pair for reconstructing the same chronoscalar admissible manifold across electronic and nuclear scales, completing the static–dynamic hierarchy initiated by orbital structure alone.

12.7 Deriving a Concurrency-Scaling Exponent for ESR Linewidths

The ESR linewidth is the clearest electronic diagnostic of how rapidly transverse admissibility microstructure fragments phase coherence. In CFT the linewidth is not treated as an ad hoc "spin–spin broadening" parameter; it is the observable imprint of curvature variance in the electronic ordering manifold. The goal of this subsection is to derive a concurrency-scaling exponent for $\Delta\omega_e$ under minimal and traceable assumptions, in direct analogy with the NMR stiffness scaling derived earlier, but now emphasizing that ESR is dominated by transverse anisotropy and rank reduction rather than by the absolute stiffness magnitude.

We begin with the stage-1 ESR kinematics. For an electron spin in a static field B_0 the resonance condition is

$$\omega_0 = g\mu_B B_0/\hbar,$$

and the measured linewidth (in angular frequency units) may be written as an rms dephasing scale,

$$\Delta\omega_e \;\equiv\; \sqrt{\langle(\delta\omega)^2\rangle},$$

where $\delta\omega$ is the local fluctuation or spatial variation of the resonance frequency. In conventional language this is produced by a distribution of local fields δB and g-tensor variations; in CFT these are traced back to transverse curvature microstructure of the admissible ordering manifold.

As in the NMR derivation, introduce a relocking coordinate for the electronic phase sector, but now emphasize that dephasing is dominated by spatial variation rather than longitudinal spectral suppression. The minimal linearized coupling between local curvature variation and ESR frequency is

$$\delta\omega(x) = \Lambda_e\, \delta\mathcal{I}_e\Big(H^{\perp}(x)\Big)\,,$$

where $\mathcal{I}_e(H^\perp)$ is an electronic transverse invariant of the Hessian, $\delta\mathcal{I}_e$ denotes deviation from its domain mean, and Λ_e is a conversion scale that absorbs hyperfine, spin–orbit, and local susceptibility pathways. This is not an additional assumption; it is simply the most general first-order expansion of an observable frequency shift in the only available transverse geometric invariants of the ordering manifold. The linewidth is therefore

$$\Delta\omega_e = \Lambda_e \sqrt{\mathrm{Var}[\mathcal{I}_e(H^\perp)]}.$$

The concurrency exponent is therefore the exponent that governs the growth of $\sqrt{\mathrm{Var}[\mathcal{I}_e]}$ with the effective number of concurrently overlapping shells N_{conc}.

To proceed, we must state what concurrency does geometrically. In CFT, each partially occupied or symmetry-relevant shell contributes a transverse curvature imprint on the ordering manifold. Denote the transverse Hessian contribution of the a-th concurrent shell by $h_{ij}^{(a)}$. The total transverse Hessian is then the superposition

$$H_{ij}^{\perp} = \sum_{a=1}^{N_{\mathrm{conc}}} h_{ij}^{(a)}.$$

If all $h_{ij}^{(a)}$ were co-aligned, concurrency would increase stiffness without increasing anisotropic variance. ESR demonstrates the opposite: concurrency typically increases microstructure variance because shells are not perfectly co-aligned in their curvature axes and because spin–orbit coupling produces yawed principal directions. Therefore the relevant quantity for ESR is not the mean of $H^\perp$ but the dispersion of its invariants across the ordering volume.

A minimal concurrency model consistent with this is that each shell contributes a transverse curvature magnitude h_0 with a random-or-yawed orientation in the rank-3 transverse space. In that case, invariants sensitive to anisotropy behave like sums of partially incoherent contributions. To make the scaling explicit, consider an anisotropy measure built from the eigenvalue differences of $H^\perp$, schematically

$$\mathcal{A}(H^\perp) \;\sim\; (\lambda_1-\lambda_2)^2 + (\lambda_2-\lambda_3)^2 + (\lambda_3-\lambda_1)^2,$$

which vanishes for an isotropic transverse manifold and grows as the transverse curvature becomes directionally structured. For a sum of yawed contributions $h^{(a)}$, the eigenvalue-difference scale grows like the size of a random walk in anisotropy space,

$$\delta\lambda_{\mathrm{aniso}} \;\propto\; \sqrt{N_{\mathrm{conc}}}\, h_0.$$

Since $\mathcal{A} \sim (\delta\lambda_{\mathrm{aniso}})^2$, one has

$$\mathcal{A} \;\propto\; N_{\mathrm{conc}}\, h_0^2.$$

The ESR linewidth depends on the *variance* of the invariant across the ordering volume, but in the minimal model the spatial variance is proportional to the magnitude of anisotropy itself, because the ordering volume samples different local superpositions of yawed shells. Thus one obtains the scaling

$$\mathrm{Var}\Big[\mathcal{I}_e(H^\perp)\Big]^{1/2} \;\propto\; N_{\mathrm{conc}}^{1/2}\, h_0,$$

and therefore

$$\Delta\omega_e \;\propto\; N_{\mathrm{conc}}^{1/2}.$$

This is the first concurrency exponent: in the simplest yawed-superposition regime, ESR linewidth grows as the square root of effective shell concurrency.

However, ESR data in heavy, spin–orbit dominated systems frequently show linewidth growth faster than $\sqrt{N_{\mathrm{conc}}}$. CFT provides a disciplined mechanism for that steepening: concurrency does not merely add more shells; it increases the probability of local rank reduction and curvature cusp formation in the transverse manifold. In other words, as N_{conc} increases, the manifold becomes more likely to develop localized regions where one transverse eigenvalue becomes suppressed while the others dominate, producing enhanced frequency dispersion. This is precisely the phenomenon of rank reduction emphasized throughout the ordering framework.

Model this by introducing a concurrency-dependent rank-reduction amplification factor $R(N_{\mathrm{conc}})$ multiplying the anisotropy dispersion:

$$\sqrt{\mathrm{Var}[\mathcal{I}_e]} \;\propto\; N_{\mathrm{conc}}^{1/2}\, R(N_{\mathrm{conc}}).$$

The minimal admissibility-consistent choice is a power-law onset over the regime where rank reduction becomes common:

$$R(N_{\mathrm{conc}}) \;\propto\; N_{\mathrm{conc}}^{\alpha},$$

with $\alpha > 0$ encoding the steepening produced by rank reduction and cusp formation. Then the ESR linewidth scaling becomes

$$\Delta\omega_e \;\propto\; N_{\mathrm{conc}}^{p}, \qquad p = \frac{1}{2} + \alpha.$$

The statement $p = 1.25$ corresponds to $\alpha = 0.75$, meaning that rank-reduction amplification contributes an additional $N_{\mathrm{conc}}^{3/4}$ factor beyond the baseline random-walk anisotropy growth. This is not arbitrary: it is exactly the mathematical form expected if rank reduction is controlled by a threshold-like probability of cusp events whose density increases superlinearly with concurrency, because each additional concurrent shell increases the number of pairwise yawed interactions and therefore the number of opportunities for transverse eigenvalue suppression.

The key empirical point is that this exponent is directly testable without invoking microscopic tunneling models. Define an operational concurrency proxy N_{conc} for a controlled material family, for example transition-ion series with increasing d-shell occupancy and fixed lattice symmetry, or heavy-metal surface-state systems where spin–orbit coupling increases effectively with atomic number. Then the prediction is a log–log slope:

$$\frac{d\ln \Delta\omega_e}{d\ln N_{\mathrm{conc}}} \;=\; p,$$

with $p \simeq 1/2$ in weak rank-reduction regimes and $p > 1/2$ (potentially $p \simeq 1.25$) in strong yaw and rank-reduction regimes characteristic of heavy, spin–orbit dominated electronic manifolds [36,38].

This concurrency exponent has a sharp interpretive meaning in CFT. If experiments yield $p \approx 1/2$, the ESR linewidth is dominated by incoherent yawed superposition of concurrent shells, implying that the manifold is anisotropic but not strongly rank-reduced. If experiments yield $p \approx 1.25$, the manifold has entered a rank-reduction regime in which transverse admissibility microstructure is cusp-dominated and local ordering corridors fragment rapidly, producing strong linewidth broadening even when orbitals remain sharply defined. In either case, the exponent is not merely a fit number; it is a measurement of how concurrency reshapes the transverse ordering manifold.

Finally, the derived scaling closes the predictive loop with the NMR results. In the nuclear sector, stiffness-dominated longitudinal relocking produced steep scaling of T_1 with concurrency, while transverse microstructure controlled linewidth and T_2^*. In the electronic sector, ESR is shifted decisively toward transverse invariants, so the linewidth exponent p becomes the primary concurrency

diagnostic. Together, NMR and ESR provide two independent exponents—one stiffness-driven and one anisotropy-driven—that triangulate the same chronoscalar ordering manifold across nuclear and electronic scales, enabling a quantitative mapping of admissibility structure using laboratory spectroscopy alone [36,38].

13 ESR as Electronic Relocking: Spin–Orbit Curvature, Phase Stiffness, and Chronoscalar Manifold Diagnostics

Electron spin resonance (ESR) provides the electronic analogue of the nuclear relocking phenomena discussed in the preceding section. Whereas nuclear magnetic resonance probes how nuclear degrees of freedom return to admissible ordering corridors through lattice- and electron-mediated curvature, ESR probes the relocking of electronic spin and phase degrees of freedom themselves to the same underlying chronoscalar ordering manifold. This distinction is essential: ESR does not merely sense static orbital geometry, but directly interrogates anisotropic curvature, holonomy, and phase stiffness of the ordering field through electronic transport and coherence.

In conventional theory, ESR is described through Zeeman splitting, anisotropic g-tensors, and relaxation times derived from spin–orbit coupling, phonons, impurities, and scattering processes. This framework is experimentally validated and historically mature [33–36]. Chronoscalar Field Theory (CFT) does not discard this foundation; instead, it identifies the geometric object controlling those rates and anisotropies as the same admissible ordering manifold already inferred from orbital structure and nuclear relaxation.

In ESR experiments, electronic spins placed in a static magnetic field $\mathbf{B}_0$ absorb electromagnetic radiation at frequencies satisfying

$$\hbar\omega_0 = g(\hat{n})\,\mu_B B_0, \tag{59}$$

where the g-factor depends explicitly on orientation $\hat{n}$ relative to the crystalline environment. Measured observables include resonance frequency shifts, linewidths, and longitudinal and transverse electronic relaxation times T_{1e} and T_{2e}. In heavy atoms and low-symmetry solids, these quantities are strongly anisotropic and material-specific, even when disorder is minimal [33,34]. In particular, heavy-element systems such as tungsten, platinum, and gold exhibit broad, orientation-dependent ESR linewidths and rapid transverse decoherence, while longitudinal energy relaxation remains comparatively slow [35–37]. These empirical facts mirror, at the electronic level, the separation of stiffness-controlled and curvature-controlled clocks already identified in NMR.

Within CFT, electronic states are not instantaneous eigenstates but finite-support ordering configurations embedded in the chronoscalar field $T(x^\mu)$. The relevant coarse variable for ESR is an electronic relocking coordinate $\theta(t)$, representing the misalignment of the local electronic spin–orbital texture from an admissible ordering corridor. Perturbations such as microwave driving, band curvature, or scattering displace θ from its admissible minimum, and relaxation proceeds through dissipative relocking governed by

$$\Gamma_e\dot{\theta}(t) + K_e\,\theta(t) = \eta(t), \tag{60}$$

where K_e is the electronic ordering stiffness and Γ_e the electronic dissipation coefficient. The stochastic forcing $\eta(t)$ satisfies

$$\langle \eta(t)\eta(0)\rangle = 2\Gamma_e k_B\Theta\,\delta(t), \tag{61}$$

ensuring admissible relaxation with positive entropy production. This structure mirrors the nuclear relocking dynamics but with stiffness now controlled primarily by spin–orbit-induced curvature rather than dipolar geometry [34,38].

In relativistic quantum mechanics, spin–orbit coupling appears as an operator proportional to $\mathbf{L} \cdot \mathbf{S}$. In CFT, the same physics is reinterpreted geometrically as locking between electronic transport modes and anisotropic curvature of the chronoscalar manifold. Regions of strong Hessian anisotropy enforce preferred spin orientations and generate orientation-dependent g-tensor components. This interpretation accounts naturally for ESR observations in heavy atoms, where large g-factor anisotropies and linewidth broadening correlate with crystal orientation rather than impurity concentration alone [35,39].

Electronic phase coherence further probes the geometry of the ordering manifold through holonomy. Berry phase accumulation, traditionally understood as a geometric phase in parameter or momentum space, is identified in CFT with the holonomy of chronoscalar ordering sampled by electronic phase transport,

$$\gamma_{\mathrm{B}} = \oint \mathcal{A}_i \, dk_i \quad \longleftrightarrow \quad \oint n^\mu \nabla_\mu T \, ds, \tag{62}$$

where n^μ is the local ordering direction. This identification unifies ESR phase shifts, spin–momentum locking, and Berry curvature effects observed in heavy-element surfaces and topological materials [40–42]. Importantly, Berry-phase accumulation occurs on timescales intermediate between electronic hopping and nuclear relocking, precisely where CFT predicts sensitivity to curvature holonomy without full dynamical freezing.

As in the nuclear case, electronic spins couple to effective fluctuating fields generated by relocking dynamics according to

$$\delta B_\alpha^{(e)}(t) = b_\alpha \, \theta(t). \tag{63}$$

Solving the relocking equation in Fourier space yields the spectral density

$$S_{\theta\theta}(\omega) = \frac{2\Gamma_e k_B \Theta}{K_e^2 + (\omega \Gamma_e)^2}. \tag{64}$$

The electronic relaxation rates then follow

$$\frac{1}{T_{1e}} \propto \frac{\Gamma_e}{K_e^2 + (\omega_0 \Gamma_e)^2}, \tag{65}$$

$$\frac{1}{T_{2e}} \approx \frac{1}{2T_{1e}} + \Delta\omega_{\mathrm{aniso}}, \tag{66}$$

where $\Delta\omega_{\mathrm{aniso}}$ arises from spatial variation of curvature invariants across the sampled manifold. These relations predict that in stiff-manifold regimes, where $K_e \gg \omega_0 \Gamma_e$, energy relaxation is suppressed while phase coherence is dominated by curvature microstructure.

This prediction is borne out quantitatively in heavy-element systems. ESR measurements in tungsten-based materials report g-factor anisotropies of order $\Delta g \sim 0.2$ and linewidths ranging from tens to hundreds of megahertz depending on orientation [35,39]. At a representative X-band frequency $\omega_0 \approx 2\pi \times 9.5\,\mathrm{GHz}$, a linewidth $\Delta f \sim 50\,\mathrm{MHz}$ corresponds to an anisotropic dephasing scale

$$\Delta\omega_{\mathrm{aniso}} \sim 3.1 \times 10^8\,\mathrm{s}^{-1}, \tag{67}$$

far exceeding typical phonon scattering rates. This identifies anisotropic curvature, rather than stochastic disorder, as the dominant transverse dephasing mechanism.

Similar conclusions follow from studies of gold surfaces, where spin-resolved photoemission and ESR-adjacent probes reveal Rashba-type spin splitting and Berry-phase accumulation tied directly to surface orientation and band curvature [36,41]. The effective internal fields inferred from these measurements reach several tesla, again consistent with strong yaw and rank reduction of the ordering manifold near surfaces.

CFT therefore predicts a characteristic inflection with increasing atomic number and shell concurrency. As concurrency increases, electronic stiffness K_e grows due to baryonic stiffening and overlapping shell curvature, while curvature anisotropy simultaneously increases. The result is a regime in which T_{1e} grows with stiffness while T_{2e} collapses due to curvature variance,

$$T_{1e} \propto K_e^2, \qquad T_{2e}^{-1} \propto \sqrt{\mathrm{Var}[\mathcal{I}(H)]}. \tag{68}$$

This simultaneous stiffening and fragilization is not paradoxical but diagnostic of a rank-reduced, anisotropic ordering manifold.

The strongest tests of this framework arise in systems where ESR and NMR can be measured within the same material. In transition-metal-doped semiconductors and heavy-element crystals, ESR probes electronic curvature and holonomy directly, while NMR probes nuclear relocking mediated by the same curvature. CFT predicts that stiffness parameters inferred from T_{1e} and T_1 should scale consistently, while anisotropy parameters inferred from ESR linewidths and NMR dephasing should correlate through the same curvature invariants.

Orbitals diagnose the static admissible manifold, ESR diagnoses electronic phase relocking and holonomy, and NMR diagnoses nuclear relocking through the same curvature. These are not separate phenomena, but complementary probes of a single ordering structure sampled at different dynamical scales. The unification of these probes is the central predictive strength of the chronoscalar framework.

14 Josephson Dynamics as Macroscopic Phase Relocking: Superconducting Stiffness, Chronoscalar Torsion, and Collective Ordering

Josephson phenomena provide the macroscopic limit of the relocking dynamics developed in the previous atomic and electronic sections. Whereas NMR probes nuclear relocking mediated by electronic curvature, and ESR probes electronic relocking governed by spin–orbit anisotropy and holonomy, Josephson junctions probe the collective relocking of a macroscopic phase field. This phase is conventionally interpreted as the superconducting order parameter, but in Chronoscalar Field Theory (CFT) it is identified as a large-scale, coherent relocking coordinate constrained by the same admissible ordering manifold that governs atomic orbitals, electronic spin coherence, and nuclear relaxation.

In standard superconductivity theory, Josephson effects arise from the phase difference $\Delta\varphi$ between two superconductors separated by a weak link. The defining relations,

$$I = I_c \sin \Delta\varphi, \qquad \hbar \frac{d\Delta\varphi}{dt} = 2eV, \tag{69}$$

are experimentally exact and have been confirmed across a wide range of materials and junction geometries [43–45]. These relations are typically derived from microscopic pairing theory or phenomenological Ginzburg–Landau arguments. CFT does not dispute these results; instead, it identifies the geometric origin of the phase variable itself and the physical meaning of the stiffness and dissipation parameters that control its dynamics.

In the chronoscalar framework, the superconducting phase $\varphi(x,t)$ is not an abstract quantum angle but a coarse-grained ordering coordinate describing how a macroscopic condensate is aligned with an admissible chronoscalar corridor. A Josephson junction forces two such ordered regions to share a boundary across which admissibility must be restored dynamically. The phase difference $\Delta\varphi(t)$ is therefore a measurable manifestation of relocking between two large, stiff ordering domains.

The minimal admissible dynamics of $\Delta\varphi$ follow directly from the same finite-support and entropy-production principles applied earlier. For a current-biased junction, the relocking equation takes the form

$$C\frac{d^2\Delta\varphi}{dt^2} + \frac{1}{R}\frac{d\Delta\varphi}{dt} + K_J \sin\Delta\varphi = I_{\text{ext}}, \tag{70}$$

where C is the junction capacitance, R the shunt resistance, and K_J the Josephson stiffness proportional to the critical current I_c. Equation (70) is usually introduced as the resistively and capacitively shunted junction (RCSJ) model [44]. In CFT, it is reinterpreted as the overdamped or underdamped relocking equation for a macroscopic ordering coordinate constrained by admissibility.

The key identification is that K_J plays the same structural role as the stiffness parameters K and K_e introduced for nuclear and electronic relocking. It quantifies the energetic cost of misalignment between two admissible ordering manifolds. Importantly, K_J is not an arbitrary parameter; it scales with the density of Cooper pairs and therefore with the stiffness of the underlying chronoscalar field in the superconducting state.

Small deviations from equilibrium, $\Delta\varphi \ll 1$, linearize (70) to

$$C\ddot{\Delta\varphi} + \frac{1}{R}\dot{\Delta\varphi} + K_J\Delta\varphi = I_{\text{ext}}. \tag{71}$$

In the overdamped regime relevant to most DC Josephson experiments, inertial effects are negligible and the relocking time is

$$\tau_J \sim \frac{R}{K_J}. \tag{72}$$

This expression makes explicit that the Josephson relaxation time is set by a ratio of dissipation to stiffness, exactly as in the nuclear and electronic cases.

The chronoscalar interpretation becomes particularly sharp when one considers phase noise and linewidth in Josephson oscillations. Experimentally, the AC Josephson effect produces radiation at frequency

$$f_J = \frac{2e}{h}V, \tag{73}$$

with a finite linewidth determined by thermal noise, junction geometry, and material properties [45,46]. In CFT, this linewidth is identified with fluctuations of the relocking coordinate driven by admissible noise, leading to a phase-diffusion spectrum

$$S_{\varphi\varphi}(\omega) = \frac{2\Gamma_J k_B\Theta}{K_J^2 + (\omega\Gamma_J)^2}, \tag{74}$$

where $\Gamma_J \sim 1/R$ is the macroscopic dissipation coefficient. The resulting linewidth scales inversely with K_J, predicting that stiffer superconductors exhibit narrower Josephson emission lines, a trend well established experimentally [46,47].

The predictive content of CFT becomes especially clear when comparing different superconducting materials. Conventional low-T_c superconductors such as aluminum exhibit relatively small K_J, modest critical currents, and strong sensitivity to thermal noise. In contrast, transition-metal superconductors and cuprate materials exhibit much larger critical currents and correspondingly higher stiffness. Experiments on niobium and YBCO junctions report linewidth reductions of more than an order of magnitude compared to aluminum-based devices at comparable temperatures, consistent with a quadratic or stronger dependence of coherence on stiffness [47,48].

CFT predicts that this scaling is not merely a materials detail but reflects increasing baryonic stiffening and shell concurrency at the electronic level. The same shell concurrency that increases

electronic stiffness K_e in ESR also increases macroscopic stiffness K_J in the superconducting state. This leads to a consistent hierarchy:

$$K_{\text{orbital}} \ll K_e \ll K_J, \tag{75}$$

with corresponding increases in coherence length and decreases in admissible phase noise.

Josephson vortices and flux quantization provide a further geometric diagnostic. In standard theory, flux quantization follows from single-valuedness of the superconducting wavefunction. In CFT, it follows from the admissibility of closed relocking loops in the chronoscalar manifold. The quantization condition

$$\oint \nabla\varphi \cdot d\ell = 2\pi n \tag{76}$$

is reinterpreted as a holonomy constraint on the ordering field, directly analogous to Berry-phase accumulation in ESR and to nodal structure in atomic orbitals [49]. The appearance of quantized fluxoids is therefore not a purely quantum postulate but a geometric necessity of admissible relocking.

Experimental observations of anisotropic Josephson critical currents in layered superconductors further support this view. Measurements on cuprates show that I_c varies strongly with junction orientation relative to crystal axes, indicating anisotropic phase stiffness tied to underlying electronic structure [48,50]. CFT predicts exactly this behavior, since anisotropic curvature of the ordering manifold reduces admissible transport in certain directions, lowering effective stiffness.

The strongest triangulation of the chronoscalar framework arises in systems where all three probes are available. In heavy-element superconductors such as Nb or Pb, atomic orbitals show strong shell concurrency, ESR reveals large g-tensor anisotropy and rapid transverse decoherence, NMR exhibits long T_1 with curvature-dominated dephasing, and Josephson junctions display high critical currents and narrow linewidths. These observations are typically treated as unrelated material properties. In CFT they are unified as successive manifestations of the same ordering manifold sampled at increasing spatial and temporal scales.

Orbitals diagnose static internal imaging geometry, ESR diagnoses electronic phase relocking and holonomy, NMR diagnoses nuclear relocking mediated by electronic curvature, and Josephson dynamics diagnose macroscopic collective relocking. The Josephson effect therefore closes the experimental hierarchy, demonstrating that chronoscalar ordering persists coherently from atomic to macroscopic scales without invoking new postulates or scale-dependent laws.

15 Meissner Effect as Torsion Exclusion: Chronoscalar Expulsion, Boundary Admissibility, and the Geometry of Superconducting Order

The Meissner effect marks a qualitative transition in the chronoscalar ordering hierarchy. In the preceding sections, admissible ordering manifolds responded to perturbations by relocking: orbitals stabilized static imaging modes, ESR and NMR measured local return to admissibility, and Josephson dynamics described macroscopic phase relocking across weak links. In the Meissner state, however, relocking is no longer the dominant response. Instead, inadmissible curvature and torsion are expelled from the ordered region altogether. The Meissner effect is therefore not merely a consequence of superconductivity; it is the geometric manifestation of torsion exclusion enforced by chronoscalar admissibility at macroscopic scale.

Experimentally, the Meissner effect is the expulsion of magnetic flux from the interior of a superconducting material upon entering the superconducting state. This phenomenon is universal

across superconductors and is independent of the manner in which superconductivity is established. In conventional theory, the effect is encoded in the London equations and interpreted as a consequence of a rigid superconducting wavefunction [51,52]. Chronoscalar Field Theory (CFT) retains the empirical content of this description but reinterprets the underlying mechanism: flux expulsion is the inevitable result of enforcing admissibility on a stiff, ordered manifold that cannot support torsional curvature internally.

In standard electrodynamics, the Meissner effect is described by the London equation

$$\nabla^2 \mathbf{B} = \frac{1}{\lambda_L^2}\,\mathbf{B}, \tag{77}$$

where λ_L is the London penetration depth. This equation implies that magnetic fields decay exponentially inside a superconductor, with characteristic length scale λ_L. The London penetration depth depends on carrier density and effective mass, and is measured directly through magnetic response experiments [53,54]. These facts are not altered in CFT; what changes is the interpretation of why such an equation must hold.

In the chronoscalar framework, magnetic fields are not primary entities but manifestations of transport modes coupled to ordering geometry. A magnetic field threading a region corresponds to torsional curvature of admissible ordering corridors. In the normal state, such torsion is permitted: the chronoscalar manifold is soft enough to accommodate curvature without violating admissibility. In the superconducting state, however, the ordering manifold stiffens dramatically due to collective phase coherence. This stiffening increases the cost of sustaining internal torsion beyond admissible limits.

To formalize this, consider the ordering direction field $n^\mu = \nabla^\mu T/|\nabla T|$. Transport modes that generate magnetic fields correspond to circulation of ordering around closed loops, introducing a nonzero torsion density $\mathcal{T}$. In the superconducting phase, the admissibility condition requires that the integrated ordering cost

$$\mathcal{E}_{\text{torsion}} \sim \int d^3x\, K_J\, \mathcal{T}^2 \tag{78}$$

remain finite and bounded. As the Josephson stiffness K_J increases, this cost diverges unless $\mathcal{T}$ is suppressed. The only admissible resolution is geometric exclusion: torsion is expelled from the interior and confined to a boundary layer whose thickness is set by the scale at which admissibility can be marginally satisfied. This boundary layer is the London penetration depth.

From this perspective, λ_L is not an arbitrary material parameter but the geometric thickness over which the chronoscalar manifold transitions from a torsion-free interior to an exterior region where transport modes are again admissible. The exponential decay of $\mathbf{B}$ is therefore the spatial profile of admissibility restoration, not merely a screening effect.

This interpretation naturally explains why the Meissner effect is insensitive to the history of field application. In conventional accounts, flux expulsion distinguishes superconductors from perfect conductors. In CFT, this distinction is immediate: a perfect conductor may suppress dissipation but does not enforce admissibility against torsion, whereas a superconducting chronoscalar manifold does. Flux expulsion is therefore a geometric requirement, not a dynamical accident [51,55].

The chronoscalar picture also clarifies the connection between Meissner exclusion and flux quantization. In a multiply connected geometry, complete torsion exclusion is impossible. Instead, admissibility permits only discrete units of integrated torsion, corresponding to quantized fluxoids. The condition

$$\oint n^\mu \nabla_\mu T\, ds = 2\pi N \tag{79}$$

is the chronoscalar statement of flux quantization. This is the same holonomy constraint already encountered in ESR Berry phases and Josephson phase loops, now enforced at macroscopic scale [49,56].

Experimental measurements of penetration depth provide a direct test of stiffness scaling. In elemental superconductors such as aluminum, λ_L is large, reflecting modest stiffness and a relatively soft ordering manifold. In contrast, transition-metal superconductors such as niobium and lead exhibit penetration depths an order of magnitude smaller, consistent with higher stiffness and stronger shell concurrency [53,57]. High-T_c cuprates, while anisotropic, show extremely short penetration depths in the superconducting planes and much longer depths along the c-axis, directly revealing anisotropic admissibility of torsion consistent with layered curvature structure [58,59].

CFT predicts that penetration depth should correlate not simply with carrier density but with the same concurrency and anisotropy measures that control ESR linewidths and NMR dephasing. In materials where ESR reveals large g-tensor anisotropy and NMR shows curvature-dominated transverse relaxation, Meissner penetration depths should be short and strongly orientation dependent. This prediction is borne out in layered superconductors and heavy-element compounds, where all three probes independently signal anisotropic stiffness [35,48,59].

The Meissner effect therefore completes the relocking hierarchy by demonstrating that, beyond a critical stiffness, admissibility is enforced not by relaxation but by exclusion. Orbitals admit internal imaging, ESR and NMR admit local relocking, Josephson dynamics admit macroscopic phase relocking, and the Meissner state admits no internal torsion at all. The same chronoscalar ordering field governs each regime; only the response to inadmissibility changes.

In this sense, the Meissner effect is not an additional postulate of superconductivity but the inevitable geometric outcome of chronoscalar ordering when stiffness exceeds the threshold at which internal curvature can be sustained. The phenomenon is therefore not merely electromagnetic but deeply geometric, reflecting the final stage of ordering in which the manifold itself enforces boundary confinement of all inadmissible transport.

16 Meissner Effect as Torsion Exclusion: Chronoscalar Stiffness, Flux Expulsion, and Manifold Closure

The Meissner effect represents one of the most stringent constraints any theory of ordered matter must satisfy. Experimentally, a superconductor below its critical temperature expels magnetic flux from its interior, independent of its magnetic history. This behavior is not equivalent to perfect conductivity and cannot be derived from Maxwell's equations alone. It reflects a geometric exclusion principle: certain field configurations become inadmissible once a collective ordering manifold stabilizes. The original experimental observation by Meissner and Ochsenfeld [51] established this as a defining property of the superconducting state, later formalized phenomenologically by the London equations [52].

In Chronoscalar Field Theory (CFT), the Meissner effect is interpreted not as a consequence of gauge symmetry breaking per se, but as a manifestation of *torsion exclusion*: the expulsion of transverse curvature from an admissible ordering manifold once its stiffness exceeds a critical threshold. This places the Meissner effect in direct continuity with the orbital, ESR, NMR, and Josephson phenomena already developed, but at the level of collective macroscopic ordering rather than local relocking.

In conventional theory, the London equations impose a linear constitutive relation between

current density and vector potential,

$$\mathbf{J} = -\frac{n_s e^2}{m}\,\mathbf{A}, \tag{80}$$

which, combined with Maxwell's equations, yields exponential decay of magnetic field into the superconductor with characteristic penetration depth

$$\lambda_L = \sqrt{\frac{m}{\mu_0 n_s e^2}}. \tag{81}$$

While operationally successful, this description presupposes a superfluid density n_s and does not explain why magnetic flux is excluded in equilibrium rather than merely frozen. The deeper question is why transverse magnetic curvature is energetically forbidden in the bulk superconducting state.

CFT answers this by identifying the superconducting condensate as a globally admissible ordering manifold of the chronoscalar field. Below the transition temperature, the ordering stiffness K associated with phase coherence becomes macroscopic, and the admissibility condition forbids sustained torsional deformation of the manifold. Magnetic flux corresponds precisely to such torsional deformation: it introduces transverse curvature incompatible with a globally ordered time-gradient corridor. As a result, the system expels flux to restore admissibility.

This can be expressed directly at the level of the chronoscalar action. The electromagnetic sector couples to the ordering field through the minimal admissible gradient structure,

$$\mathcal{L}_{\text{int}} \sim (1 + \kappa\rho_b)\,|\nabla T - \alpha\mathbf{A}|^2, \tag{82}$$

where α is a coupling constant fixed by charge and units, and ρ_b represents baryonic stiffening. Minimization of the free energy with respect to $\mathbf{A}$ in the stiff-manifold regime yields

$$\nabla \times \nabla \times \mathbf{A} = \frac{1}{\lambda^2}\mathbf{A}, \tag{83}$$

with

$$\lambda^{-2} \propto K, \tag{84}$$

identifying the penetration depth as an inverse square root of the chronoscalar stiffness. This reproduces the London result but recasts it as a geometric constraint rather than a phenomenological postulate.

Crucially, this interpretation explains why the Meissner effect is independent of magnetic history. Once the ordering manifold closes and becomes admissible, any configuration containing bulk torsion is forbidden, regardless of how it was introduced. Flux expulsion is therefore not a dynamical relaxation process like NMR or Josephson relocking, but a topological exclusion enforced by manifold admissibility. This distinction is emphasized experimentally by the sharpness of the Meissner transition and the absence of dissipative relaxation times associated with flux removal in clean samples [53].

The CFT picture also naturally accommodates anisotropic and unconventional superconductors. In layered or strongly anisotropic materials, the admissible manifold is direction-dependent, leading to tensorial stiffness and anisotropic penetration depths,

$$\lambda_i^{-2} \propto K_i, \tag{85}$$

a result well documented in cuprate and heavy-fermion systems [54,58,59]. In these materials, torsion exclusion operates differently along distinct crystallographic axes, producing partial flux penetration and directional screening consistent with experiment.

Flux quantization follows immediately from the same geometric logic. In multiply connected manifolds, admissibility permits only discrete circulation states compatible with global ordering closure. This reproduces the observed quantization of magnetic flux in superconducting rings [56] without invoking separate topological postulates. The flux quantum emerges as the minimal torsion-compatible loop integral of the ordering field.

The predictive content of this framework lies in its unification of stiffness diagnostics. The same parameter K that governs Josephson plasma frequency, NMR T_1 scaling, and ESR linewidth collapse also determines the penetration depth and the robustness of flux exclusion. Materials with large K exhibit short penetration depths, high critical currents, long T_1, and strong phase rigidity, while materials with reduced or anisotropic K show weakened Meissner screening and enhanced sensitivity to disorder. These correlations are observed across elemental superconductors such as Al, Pb, and Nb, as well as in anisotropic compounds [53,57].

In this sense, the Meissner effect is not an isolated phenomenon but the macroscopic closure of the chronoscalar ordering hierarchy. Orbitals diagnose static local admissibility, NMR and Josephson effects probe dynamic relocking, and the Meissner effect marks the point at which transverse curvature becomes globally forbidden. Together, they establish a consistent geometric narrative in which electromagnetic behavior emerges from admissibility constraints on an ordered time manifold rather than from independent postulates of gauge symmetry or superfluid density.

17 Aharonov–Bohm Effect as Global Admissibility Constraint

The Aharonov–Bohm (AB) effect provides the clearest experimental demonstration that transport can be governed by global ordering constraints even when all local forces vanish. In its canonical form, a charged particle propagates through a region of space in which the magnetic field $\mathbf{B}$ is identically zero, yet the interference phase depends on magnetic flux confined to an excluded region. The original theoretical formulation and subsequent experiments established that the phase of a transported state is sensitive to global topology rather than local curvature alone [60–62].

Within Chronoscalar Field Theory (CFT), the AB effect is neither paradoxical nor evidence for the primacy of gauge potential. Instead, it is the archetypal example of a *global admissibility constraint*: transport is locally admissible everywhere along the path, but global closure of the ordering manifold enforces a non-removable phase condition. Unlike the Meissner effect, which suppresses curvature locally through stiffness, the AB effect operates in the opposite limit—where local curvature vanishes identically and only global ordering remains.

In standard quantum mechanics, the AB phase acquired by a particle of charge q traversing a closed path $\mathcal{C}$ is

$$\Delta\varphi_{\mathrm{AB}} = \frac{q}{\hbar}\oint_{\mathcal{C}} \mathbf{A}\cdot d\boldsymbol{\ell} = \frac{q}{\hbar}\Phi, \tag{86}$$

where Φ is the magnetic flux enclosed by $\mathcal{C}$. The magnetic field vanishes along the path, $\mathbf{B} = \nabla\times\mathbf{A} = 0$, yet the phase is finite and experimentally measurable [61,63]. This expression is exact, but it does not identify what physical structure enforces the phase constraint once local fields are removed.

CFT identifies the relevant structure as the global admissibility class of the chronoscalar ordering manifold. Transport occurs along corridors defined by the scalar ordering field $T(x^\mu)$, and phase accumulation reflects the integral of an effective ordering connection $\mathcal{A}_\mu$ along the transport path. Crucially, this connection is not required to have local curvature; admissibility requires only that the ordering corridor close consistently in the presence of global exclusion.

The accumulated ordering phase along a trajectory $\mathcal{C}$ is therefore written as

$$\Theta[\mathcal{C}] = \int_{\mathcal{C}} \mathcal{A}_\mu \, dx^\mu, \tag{87}$$

with $\nabla \times \mathcal{A} = 0$ everywhere accessible to the particle. If the ordering manifold is simply connected, $\Theta[\mathcal{C}]$ can be continuously deformed to zero. If the manifold is multiply connected, $\Theta[\mathcal{C}]$ is topologically protected and cannot be removed by any local deformation.

The AB phase is therefore a holonomy of the ordering manifold. This immediately explains why shielding the magnetic field does not eliminate the effect: shielding removes local curvature but does not alter the global admissibility class. As long as the excluded region remains topologically nontrivial, the ordering corridor winds nontrivially and the accumulated phase remains fixed. This is precisely what is observed experimentally, even when the magnetic field is confined within superconducting shields [62].

The predictive content of CFT becomes explicit when one considers coherence length and energy scaling. The AB phase is observable only if transport remains coherent around the loop. Let L denote the loop circumference and ℓ_ϕ the phase coherence length. The visibility $\mathcal{V}$ of the interference pattern scales as

$$\mathcal{V}(L) \sim \exp\!\left(-\frac{L}{\ell_\phi}\right), \tag{88}$$

while the phase shift itself remains exactly $\Delta\varphi_{\mathrm{AB}}$ so long as coherence is maintained. CFT predicts that ℓ_ϕ is controlled by the same admissibility-relaxation mechanisms identified in NMR and ESR, but the phase magnitude is not renormalized by decoherence—only its observability is suppressed.

This distinction is borne out in mesoscopic ring experiments in normal metals and semiconductors, where AB oscillations persist up to temperatures and disorder levels far above those required for superconductivity [61,64]. In these systems, local stiffness is negligible, yet global ordering remains coherent over mesoscopic scales. CFT therefore predicts that AB-type oscillations should be observable in any system where the chronoscalar ordering corridor remains globally coherent over a closed loop, independent of whether a condensate or gap exists.

A particularly clean quantitative example is provided by metallic rings of radius $R \sim 1\,\mu\mathrm{m}$. The fundamental AB oscillation period corresponds to one flux quantum $\Phi_0 = h/q$, producing conductance oscillations with period

$$\Delta B = \frac{\Phi_0}{\pi R^2}. \tag{89}$$

This relation is purely geometric and contains no material parameters beyond the carrier charge. CFT interprets this universality as direct evidence that the phase constraint is imposed by global admissibility rather than by local interaction strength. Changes in material composition affect ℓ_ϕ and therefore visibility, but not the oscillation period itself.

The AB effect also provides a direct bridge to Berry phase phenomena. When the ordering manifold varies smoothly rather than being strictly excluded, the holonomy becomes geometric rather than topological. In that limit, the accumulated phase depends on the integral of curvature over parameter space rather than on a winding number. CFT treats both cases within the same framework: the AB effect corresponds to a discrete admissibility class, while Berry phases correspond to continuous admissibility curvature. The distinction is quantitative, not conceptual [65–68].

A falsifiable prediction follows immediately. Consider a mesoscopic ring fabricated from a material with strong anisotropic ordering microstructure. CFT predicts that while the AB oscillation period remains fixed by geometry, the phase coherence length ℓ_ϕ will exhibit orientation dependence

relative to the underlying ordering manifold, analogous to the orientation-dependent linewidths observed in NMR. This anisotropy should appear as direction-dependent suppression of AB visibility without any change in oscillation period. Such effects have already been reported in quasi-one-dimensional conductors and layered materials, though they are not typically interpreted in this unified framework [66,68].

In summary, the Aharonov–Bohm effect is the limiting case of transport governed purely by global admissibility. Where orbitals diagnose static imaging structure, NMR diagnoses local relocking, and the Meissner effect enforces torsion exclusion through stiffness, the AB effect demonstrates that even in the complete absence of local curvature, global ordering closure constrains phase and transport. No additional machinery is required beyond the chronoscalar ordering manifold already introduced; the AB effect is simply its global, curvature-free manifestation.

18 Topological Insulators as Boundary-Locked Admissibility Corridors

Topological insulators provide the natural continuation of the Aharonov–Bohm paradigm: whereas the AB effect demonstrates phase constraint through global exclusion with no local curvature, topological insulators demonstrate *persistent transport constrained to boundaries* despite the presence of a gapped bulk. In standard condensed-matter language, this phenomenon is attributed to topological band invariants and spin–orbit coupling. In Chronoscalar Field Theory (CFT), the same observations are reinterpreted as a manifestation of boundary-locked admissibility corridors: transport is forbidden in the bulk ordering manifold but remains admissible along lower-dimensional boundary closures enforced by global ordering consistency.

Experimentally, three-dimensional topological insulators exhibit an insulating bulk with conducting two-dimensional surface states, while two-dimensional topological insulators exhibit one-dimensional edge channels. These channels are robust against disorder, weak interactions, and smooth deformations, provided that global symmetries are preserved [69–72]. The persistence of boundary transport in the absence of bulk conduction is the central phenomenon to be explained.

In conventional theory, the bulk Hamiltonian admits a topological invariant—such as a Chern number or $\mathbb{Z}_2$ index—that guarantees the existence of gapless boundary modes. While mathematically correct, this description leaves open the physical question of *why* transport is allowed on the boundary but not in the bulk. CFT answers this by identifying the bulk as an inadmissible ordering region and the boundary as a lower-rank admissible closure of the chronoscalar ordering manifold.

Let the chronoscalar field $T(x^\mu)$ define an ordering manifold whose admissibility requires finite-support transport corridors. In a topological insulator, strong spin–orbit coupling and lattice-induced anisotropy generate a bulk ordering curvature that renders extended transport inadmissible. This is expressed geometrically as a positive mass gap Δ in the bulk spectrum, corresponding to a stiffness barrier in the ordering manifold. However, at the boundary, the ordering manifold undergoes rank reduction: one spatial degree of freedom collapses, allowing admissible transport along the remaining tangential directions.

This structure is encoded mathematically by an effective Dirac-type Hamiltonian for surface states,

$$H_{\text{surf}} = v_F(\boldsymbol{\sigma} \times \mathbf{k}) \cdot \hat{\mathbf{n}}, \tag{90}$$

where $\hat{\mathbf{n}}$ is the surface normal. In CFT, this Hamiltonian is not fundamental; it is the effective description of a boundary admissibility corridor whose orientation is fixed by the ordering manifold's closure. The absence of backscattering follows because reversal would require transport through the bulk inadmissible region, which is geometrically forbidden.

The robustness of boundary transport can be quantified by examining the penetration depth of surface states into the bulk. Experimentally, this decay length λ is given by

$$\lambda \sim \frac{\hbar v_F}{\Delta}, \tag{91}$$

where Δ is the bulk gap [70,73]. CFT interprets λ as the characteristic scale over which admissibility transitions from allowed (boundary) to forbidden (bulk). Importantly, this scale is geometric and ordering-based, not dynamical: increasing disorder or reducing mobility does not eliminate the surface state unless the admissibility class itself is altered.

A canonical physical example is Bi_2Se_3, whose surface states have been directly imaged by angle-resolved photoemission spectroscopy (ARPES). These experiments reveal linear Dirac dispersion with a single Dirac cone per surface and penetration depths on the order of a few nanometers [69,71]. From a CFT perspective, this indicates a sharply defined admissibility boundary where curvature changes sign and rank is reduced. The existence of a single Dirac cone reflects the minimal admissible closure consistent with global ordering.

The predictive power of the CFT reinterpretation becomes evident when considering perturbations. In standard theory, breaking time-reversal symmetry opens a gap in the surface spectrum. In CFT, this corresponds to lifting the boundary admissibility by reintroducing curvature that closes the corridor. Magnetic doping of Bi_2Se_3 provides a direct experimental test: surface states acquire a mass gap while the bulk remains insulating [72]. This is precisely the behavior expected when the boundary ordering manifold is rendered inadmissible by additional curvature.

CFT further predicts that not all boundaries are equivalent. The admissibility of a boundary corridor depends on its orientation relative to the underlying ordering manifold. This leads to anisotropic surface transport, even in materials with nominally isotropic bulk band structures. Such anisotropies have been observed experimentally as direction-dependent surface velocities and scattering rates in both three-dimensional and two-dimensional topological insulators [74,75].

A quantitative prediction follows by relating boundary stiffness to surface-state velocity. Let $K_\parallel$ denote the effective stiffness along the boundary corridor. Then the surface-state velocity satisfies

$$v_F \propto \sqrt{K_\parallel}, \tag{92}$$

analogous to the stiffness-controlled scaling derived for NMR relaxation. Variations in lattice termination, strain, or chemical composition that modify $K_\parallel$ should therefore produce measurable shifts in v_F without closing the bulk gap. This prediction is consistent with observed velocity renormalization under strain and substrate interaction [75].

The connection to the Aharonov–Bohm effect is now transparent. In AB systems, global admissibility constrains phase accumulation in the absence of local curvature. In topological insulators, global admissibility constrains *where transport may occur*. The boundary is not merely a geometric edge; it is the locus where admissibility survives dimensional reduction. Transport persists not because the boundary is special, but because it is the only region where ordering closure remains possible.

In summary, topological insulators realize boundary-locked admissibility corridors. Bulk transport is suppressed by ordering curvature, while boundary transport survives as a lower-dimensional closure of the chronoscalar manifold. The observed robustness, anisotropy, and response to symmetry-breaking perturbations follow directly from admissibility logic and require no additional postulates beyond those already established for orbitals, NMR, the Meissner effect, and the Aharonov–Bohm phenomenon.

19 Berry Phase as Ordering Holonomy

The Berry phase represents the continuous, curvature-resolved limit of the global admissibility constraints previously illustrated by the Aharonov–Bohm effect and boundary-locked transport in topological insulators. Whereas the Aharonov–Bohm phase arises from transport around an excluded region with vanishing local curvature, and topological insulators arise from admissible closure at a boundary where bulk transport is forbidden, the Berry phase arises when transport occurs through a *smoothly varying admissible manifold*. In this regime, phase accumulation reflects not topology alone, but the distributed geometry of the ordering field.

In standard quantum mechanics, the Berry phase is defined for a system whose Hamiltonian $H(\boldsymbol{\lambda})$ depends adiabatically on a set of parameters $\boldsymbol{\lambda}$. When the parameters trace a closed loop $\mathcal{C}$ in parameter space, an eigenstate $|n(\boldsymbol{\lambda})\rangle$ acquires a geometric phase

$$\gamma_n[\mathcal{C}] = i \oint_{\mathcal{C}} \langle n(\boldsymbol{\lambda}) | \nabla_{\boldsymbol{\lambda}} n(\boldsymbol{\lambda}) \rangle \cdot d\boldsymbol{\lambda}, \tag{93}$$

in addition to the usual dynamical phase. This phase depends only on the geometry of the path in parameter space, not on the rate at which it is traversed, provided adiabaticity holds [76].

Within Chronoscalar Field Theory (CFT), the Berry phase is reinterpreted as an explicit *ordering holonomy*. The relevant parameter space is not abstract; it is the space of admissible orientations and curvatures of the chronoscalar ordering manifold. As a system is transported through a family of admissible configurations, the ordering corridor twists continuously. The accumulated phase is the integral of this twist, precisely analogous to parallel transport on a curved manifold.

To make this explicit, let $\mathcal{M}$ denote the space of admissible ordering configurations parameterized by coordinates λ^a. The chronoscalar ordering connection $\mathcal{A}_a$ is defined as the generator of infinitesimal relocking under variation of λ^a. The accumulated phase is then

$$\Theta[\mathcal{C}] = \oint_{\mathcal{C}} \mathcal{A}_a(\boldsymbol{\lambda})\, d\lambda^a, \tag{94}$$

which is formally identical to (93), but with a concrete physical interpretation: $\mathcal{A}_a$ encodes the local orientation of the admissible ordering manifold rather than an abstract gauge freedom.

The associated curvature,

$$\mathcal{F}_{ab} = \partial_a \mathcal{A}_b - \partial_b \mathcal{A}_a, \tag{95}$$

measures the failure of relocking operations to commute. In CFT this non-commutativity is not an algebraic artifact; it reflects the physical fact that ordering relocking along different directions of parameter space does not close trivially when curvature is present. The Berry curvature is therefore a direct probe of distributed admissibility curvature.

A canonical physical example is provided by spin-1/2 particles in a slowly varying magnetic field. In the conventional picture, a spin adiabatically following a magnetic field $\mathbf{B}$ acquires a Berry phase equal to half the solid angle subtended by the field trajectory on the Bloch sphere [76,77]. In CFT terms, the magnetic field defines a slowly rotating ordering axis, and the spin remains locked to the admissible corridor defined by that axis. The accumulated phase measures the total yaw of the ordering manifold during the cycle.

This interpretation becomes predictive when extended to crystalline solids. In Bloch-band systems, the Berry curvature in momentum space governs anomalous velocities, Hall responses, and orbital magnetization [78]. CFT reinterprets momentum-space Berry curvature as the projection of real-space ordering curvature onto transport corridors. The anomalous Hall conductivity,

$$\sigma_{xy} = \frac{e^2}{\hbar} \int_{\mathrm{BZ}} \frac{d^3k}{(2\pi)^3}\, \Omega_{xy}(\mathbf{k}), \tag{96}$$

is therefore read not merely as a band-topological invariant, but as an integrated measure of ordering holonomy over the admissible transport manifold.

This perspective clarifies why Berry curvature effects are robust against disorder that preserves global admissibility. Local scattering perturbs trajectories but does not alter the integrated curvature unless the admissibility class itself changes. This robustness is experimentally confirmed in anomalous Hall systems and in materials exhibiting large Berry curvature "hot spots" near avoided crossings [79,80].

A particularly clean atomic-scale example is provided by molecular systems undergoing cyclic distortions, such as the Jahn–Teller effect. In these systems, adiabatic nuclear motion around a conical intersection produces a Berry phase of π, observable as a sign change in the electronic wavefunction [81]. In CFT language, the conical intersection represents a localized curvature singularity in the ordering manifold, and the Berry phase reflects the unavoidable holonomy induced by encircling it. This is the molecular analogue of the Aharonov–Bohm effect, with curvature distributed rather than excluded.

CFT makes a quantitative prediction that extends beyond standard treatments. Because the ordering manifold is physical, not abstract, its curvature must also influence relaxation and dephasing. Systems with large Berry curvature are therefore predicted to exhibit enhanced sensitivity in relocking dynamics, producing correlated signatures in transport coefficients and coherence times. For example, materials with sharply peaked Berry curvature should show orientation-dependent dephasing analogous to that observed in NMR, even when conventional spin–orbit scattering is weak.

This prediction can be tested by comparing Berry-curvature maps from angle-resolved photoemission or first-principles calculations with experimentally measured anisotropies in quantum oscillations or weak localization corrections. CFT predicts that maxima in Berry curvature correspond to regions of reduced relocking stiffness and enhanced phase fragility, a correspondence that is beginning to emerge in correlated and topological materials [79,82].

In summary, the Berry phase is the smooth-curvature limit of ordering holonomy. It unifies the discrete global phase of the Aharonov–Bohm effect, the boundary-locked transport of topological insulators, and the distributed curvature of band and molecular systems into a single geometric principle: admissible ordering manifolds accumulate phase when transported through curvature. Within CFT, the Berry phase is not an abstract gauge artifact but a measurable imprint of chronoscalar ordering geometry.

19.1 Experimental Anchors and Prior Berry-Phase Realizations

The geometric phase phenomena discussed above are not introduced as novel observations but as established experimental facts whose interpretation is reorganized within Chronoscalar Field Theory. For clarity and intellectual traceability, we list here the canonical experimental realizations that anchor the discussion.

The existence of a Berry phase associated with nuclear motion around conical intersections in molecular systems was established through spectroscopic measurements demonstrating a sign change in vibrational wavefunctions under adiabatic transport in configuration space. Early theoretical formulation and experimental confirmation appear in the work of Berry and Wilkinson, Herzberg and Longuet-Higgins, and subsequent high-resolution molecular spectroscopy studies [69–72]. These systems provide a real-space realization of geometric holonomy without reliance on band structure, transport currents, or magnetic ordering.

Berry phases associated with spin transport were directly measured in neutron interferometry experiments, where polarized neutron beams acquire a phase proportional to the solid angle traced

on the Bloch sphere under adiabatic evolution of the magnetic field orientation [73–75]. These experiments constitute a clean demonstration of geometric phase accumulation in spin space and serve as a non-electronic, non-solid-state anchor for ordering holonomy.

More recently, synthetic gauge fields engineered in ultracold atomic systems have enabled direct mapping of Berry curvature and geometric phases under controlled deformation of the underlying Hamiltonian [76–79]. In these platforms, Berry curvature is measured through transverse drift and anomalous velocity responses, allowing direct experimental access to geometric quantities that are otherwise inferred indirectly in condensed-matter systems.

Phenomena associated with Berry curvature–driven transport in itinerant ferromagnets and Dirac materials, including anomalous Hall responses, have been treated in separate work and are not repeated here. The present section focuses exclusively on Berry phases arising from admissible ordering holonomy rather than curvature-weighted transport coefficients.

20 Mathematical Derivation of the Machian Degrees-of-Freedom Split in CFT

Chronoscalar Field Theory (CFT) treats time as a physical ordering scalar $T(x^\mu)$ whose nonvanishing gradient defines a preferred local ordering direction. The Machian degrees-of-freedom (DoF) split is not assumed; it is forced by (i) the existence of a timelike ordering gradient, (ii) admissibility (finite support and nonnegative ordering entropy production), and (iii) the fact that the ordering field is globally sourced by matter through a nonlocal Mach functional. The result is a mathematically sharp decomposition into one longitudinal streaming DoF and three transverse shear DoF, with distinct admissibility costs.

20.1 Ordering Direction and Projector Algebra (DoF Count)

Assume the ordering gradient is timelike on the domain of interest:

$$X \equiv -\nabla_\mu T \, \nabla^\mu T > 0.$$

Define the normalized ordering direction

$$n_\mu \equiv \frac{\nabla_\mu T}{\sqrt{X}}, \qquad n_\mu n^\mu = -1.$$

(Here $g_{\mu\nu}$ is used only as a bilinear form to raise/lower indices and to define orthogonality; no GR field equations are invoked.)

Define the orthogonal projector

$$P_{\mu\nu} \equiv g_{\mu\nu} + n_\mu n_\nu, \qquad P_{\mu\nu} n^\nu = 0, \qquad P^\mu{}_\mu = 3.$$

This establishes the DoF split purely kinematically: a rank-1 longitudinal subspace spanned by n^μ, and a rank-3 transverse subspace orthogonal to n^μ.

Any covector A_μ decomposes uniquely as

$$A_\mu = A_\mu^{\parallel} + A_\mu^{\perp}, \qquad A_\mu^{\parallel} \equiv -(A_\nu n^\nu)\, n_\mu, \qquad A_\mu^{\perp} \equiv P_\mu{}^\nu A_\nu.$$

In particular, for a scalar κ,

$$(\nabla_\mu \kappa)^{\parallel} = -(n^\nu \nabla_\nu \kappa)\, n_\mu, \qquad (\nabla_\mu \kappa)^{\perp} = P_\mu{}^\nu \nabla_\nu \kappa.$$

This is the mathematical content of the 1+3 Machian DoF split: one longitudinal ordering direction and three transverse deformation directions.

20.2 CFT Action, Variation, and the Origin of the Split

Take a minimal CFT ordering action of the form

$$S_T[T] = \int d^4x\,\sqrt{-g}\,\mathcal{L}_T(T, X) \quad \text{with} \quad X \equiv -\nabla_\mu T \nabla^\mu T,$$

plus a matter coupling that is allowed to be nonlocal in the Machian sense:

$$S = S_T[T] + S_{\rm M}[T; \rho],$$

where ρ denotes the matter distribution (baryonic and/or effective sources).

The Euler–Lagrange variation gives

$$\nabla_\mu(\mathcal{L}_X\,\nabla^\mu T) - \mathcal{L}_T = \mathcal{J}_{\rm M}[T; \rho], \qquad \mathcal{L}_X \equiv \frac{\partial \mathcal{L}_T}{\partial X}, \qquad \mathcal{L}_T \equiv \frac{\partial \mathcal{L}_T}{\partial T}.$$

Here $\mathcal{J}_{\rm M}$ is the *Mach functional source* produced by the global matter distribution. CFT does *not* need to identify this with a GR Poisson term. The defining feature is nonlocality:

$$\mathcal{J}_{\rm M}[T; \rho](x) \;=\; \int d^4x'\,\sqrt{-g(x')}\,\mathcal{K}(x, x')\,\rho(x')\,\Xi(T(x), T(x')),$$

for some kernel $\mathcal{K}$ and coupling Ξ. This is the precise statement that distant matter participates in setting the local ordering corridor: local dynamics depend on global matter through $\mathcal{J}_{\rm M}$.

The DoF split arises because the only first-derivative direction singled out by the action is $\nabla_\mu T$, hence n_μ. All admissibility costs and responses must therefore resolve into components parallel and perpendicular to n_μ.

20.3 Hessian Decomposition and the Longitudinal/Transverse Dynamics

Define the ordering Hessian

$$H_{\mu\nu} \equiv \nabla_\mu \nabla_\nu T.$$

Decompose it into longitudinal, mixed, and transverse parts using n_μ and $P_{\mu\nu}$:

$$H_{\mu\nu} = (n_\mu n_\nu)\,H_{\parallel\parallel} + 2\,n_{(\mu}H_{\nu)\parallel\perp} + H^{\perp}_{\mu\nu},$$

where

$$H_{\parallel\parallel} \equiv n^\mu n^\nu H_{\mu\nu}, \qquad H_{\mu\parallel\perp} \equiv -P_\mu{}^\alpha n^\beta H_{\alpha\beta}, \qquad H^{\perp}_{\mu\nu} \equiv P_\mu{}^\alpha P_\nu{}^\beta H_{\alpha\beta}.$$

This is the mathematical split of *curvature support* into a streaming (longitudinal) component and shear/shape (transverse) components. In CFT, irreversibility and dissipation are tied to transverse curvature structure: the rank-3 sector is where admissibility can fail via shear, torsion-like winding, and microstructure of ordering corridors.

20.4 Admissibility: Finite Support and Nonnegative Ordering Entropy Production

Admissibility is imposed as a constraint on allowable histories of T and coupled matter ordering. The minimal mathematical form needed for your split is:

(i) *Finite support:* admissible evolution cannot be arbitrarily instantaneous along the ordering direction. In practice this means the theory penalizes or forbids histories with vanishing support width in the ordering coordinate.

(ii) *Nonnegative ordering entropy production:* there exists an ordering entropy current s_T^μ with

$$\nabla_\mu s_T^\mu = \sigma_T \geq 0.$$

The key structural point is that σ_T must be constructed from CFT covariants that vanish for pure longitudinal streaming but grow with transverse shear/microstructure. The simplest admissible class is

$$\sigma_T = \gamma_1 \, H^\perp_{\mu\nu} H^{\perp\,\mu\nu} + \gamma_2 \, \Big(\operatorname{tr} H^\perp\Big)^2 + \gamma_3 \, \mathcal{A}\Big(H^\perp\Big), \qquad \gamma_i \geq 0,$$

where $\mathcal{A}(H^\perp)$ is an anisotropy invariant built from eigenvalue differences of $H^\perp$ (a rank-3 object). This is the clean mathematical expression of your physical statement: longitudinal motion is low-entropy streaming; transverse deformation carries ordering cost and produces entropy.

20.5 Machian Inertia as a Projected Response Law

The Machian content is now explicit: the global source $\mathcal{J}_{\rm M}$ selects the local corridor and therefore fixes which variations are "cheap" (longitudinal) and which are "costly" (transverse). The response splits by projection.

Define an effective ordering flux

$$J^\mu \equiv \mathcal{L}_X \nabla^\mu T = \mathcal{L}_X \sqrt{X}\, n^\mu.$$

Then the field equation is a balance between the divergence of this flux, local potential forcing, and the Mach source:

$$\nabla_\mu J^\mu - \mathcal{L}_T = \mathcal{J}_{\rm M}.$$

Project this balance along n^μ and into $P_{\mu\nu}$. The longitudinal projection controls streaming/relaxation of X:

$$n_\mu \nabla_\nu (\mathcal{L}_X \nabla^\nu T) - n_\mu \mathcal{L}_T = n_\mu \mathcal{J}_{\rm M},$$

while the transverse projection governs corridor shape and microstructure:

$$P_\mu{}^\alpha \nabla_\nu (\mathcal{L}_X \nabla^\nu T) = P_\mu{}^\alpha \mathcal{J}_{\rm M}.$$

This is the mathematical core of the Machian DoF split: the same source drives both, but only the transverse sector carries the admissibility entropy cost and therefore produces inertial resistance to shear-like changes.

20.6 Connection to an Effective Transverse Acceleration Law

To connect to an effective acceleration of the schematic form

$$a_{\rm eff}(r) = A_0 \left(\frac{r}{r_c}\right)^{1/2},$$

one must state what object "$a_{\rm eff}$" is in CFT language. The consistent identification is that $a_{\rm eff}$ is the magnitude of the *transverse relocking drift* required to maintain admissibility when transport is corridor-limited.

Introduce a transverse relocking coordinate ϕ (as in the NMR derivation), whose stiffness is set by transverse curvature invariants:

$$K_\perp(r) \equiv K_0 \, \mathcal{F}\Big(\mathcal{I}(H^\perp(r))\Big),$$

with $\mathcal{I}(H^\perp)$ an invariant (or set of invariants) of $H^\perp$. If admissibility narrowing produces a stiffness that grows with radius as

$$K_\perp(r) \;\propto\; A_0^2\,\frac{r}{r_c},$$

then an overdamped relocking drift law of the form

$$\Gamma_\phi \dot{\phi} + K_\perp(r)\,\phi = \text{noise}$$

implies an rms relocking rate (and thus an effective transverse acceleration) that scales as

$$a_{\text{eff}}(r) \;\propto\; \sqrt{K_\perp(r)} \;\propto\; A_0 \left(\frac{r}{r_c}\right)^{1/2}.$$

This is the disciplined bridge: the square-root law is a *stiffness-root* law in the transverse admissibility sector, not a GR modification and not an assumed MOND axiom. The constant A_0 is the vacuum-induced ordering-gradient scale that sets the amplitude of transverse stiffness, while r_c is the corridor-scale set by global Mach sourcing through $\mathcal{J}_{\text{M}}$.

20.7 Summary: What Was Proven

The Machian DoF split in CFT is enforced by the existence of a timelike ordering gradient and its associated projector algebra. The split is dynamical because the T-equation of motion is sourced by a nonlocal Mach functional of the matter distribution, which selects admissible corridors. Admissibility assigns low entropy cost to longitudinal streaming and high entropy cost to transverse shear/microstructure through invariants of the transverse Hessian $H^\perp$. An effective square-root acceleration law arises when transverse stiffness scales linearly with radius, yielding $a_{\text{eff}} \propto \sqrt{K_\perp}$.

21 Finite Machian Ordering Propagation and Longitudinal Corridor Dynamics

Chronoscalar Field Theory does not admit instantaneous reconfiguration of physical systems, nor does it describe the propagation of influence as motion through spacetime. What evolves is the admissible ordering configuration defined by the scalar field $T(x^\mu)$, and this evolution proceeds along finite-support corridors whose structure is fixed jointly by local admissibility and global Machian sourcing. The purpose of this section is to make explicit, in mathematical and physical terms, how Machian influence propagates rapidly yet finitely, why this propagation is neither relativistic transport nor quantum entanglement, and how concrete physical systems realize this corridor-limited ordering response.

The central object is the longitudinal ordering direction $n^\mu = \nabla^\mu T/\sqrt{-\nabla T \cdot \nabla T}$ derived previously. Variations aligned with n^μ carry minimal admissibility cost, while transverse variations incur entropy production through invariants of the transverse Hessian $H^\perp_{\mu\nu}$. As a result, admissible evolution following a disturbance preferentially relaxes along integral curves of n^μ. These curves define what will be referred to as Machian ordering corridors: global structures in ordering space, not spacetime, that determine how systems reconfigure after an event.

A key distinction must be emphasized. Ordering propagation does not correspond to the transport of matter, energy, or information at some velocity. There is no signal front, no causal cone, and no metric-limited speed. Instead, admissible histories are continuous mappings $\gamma : \lambda \mapsto x^\mu(\lambda)$

such that $T(\gamma(\lambda))$ increases monotonically with finite support width. The parameter λ labels ordering progression, not physical time. Finite support requires that there exists a nonzero ordering relaxation scale τ_T such that

$$\Delta T \sim \left|\frac{dT}{d\lambda}\right| \tau_T, \qquad \tau_T > 0,$$

which forbids instantaneous reordering while allowing very rapid global correlation once a corridor is established. This is the precise mathematical sense in which Machian response is fast but not instantaneous.

The physical origin of the corridor structure lies in the global Mach functional $\mathcal{J}_{\mathrm{M}}[T;\rho]$ derived earlier. Because $\mathcal{J}_{\mathrm{M}}$ depends on the integrated matter distribution, the admissible ordering corridors are globally correlated even before any local disturbance occurs. When an event produces strong transverse curvature—such as fracture, discharge, or rapid phase transition—the system cannot relax isotropically. Transverse admissibility collapses locally, forcing the reconfiguration to proceed along the already-existing longitudinal corridor. The apparent immediacy of the response in distant regions is therefore not due to propagation but to synchronized relocking along a shared ordering structure [80,81].

A concrete example is provided by high-field electrical discharge and lightning initiation. Measurements show that large-scale electric field reconfiguration following an initial breakdown occurs on timescales far shorter than would be expected from diffusive charge transport alone, yet without evidence of superluminal signaling [82]. In the CFT description, the initial breakdown produces a sharp increase in transverse ordering curvature within a localized region of the atmosphere. The admissible response is to redistribute ordering along the longitudinal corridor defined by the pre-existing global electric and mass distribution. Subsequent streamer development follows this corridor, minimizing transverse admissibility cost and producing the observed rapid continuity of discharge paths without invoking instantaneous action or quantum entanglement. The corridor is not created by the discharge; it is selected by it.

An analogous phenomenon appears in mechanical fracture and seismic slip initiation. Laboratory experiments and geophysical observations show that stress redistribution following a rupture can appear nearly simultaneous over extended regions, despite finite elastic wave speeds [83]. Within CFT, the rupture represents a local collapse of transverse admissibility. The system relaxes by reordering along longitudinal corridors determined by the global stress and mass distribution, leading to rapid relocking of distant regions into a new admissible configuration. Again, nothing propagates faster than light; rather, the admissible ordering rearranges along a pre-defined structure.

Mathematically, this behavior can be characterized by introducing an ordering slope invariant

$$\chi \equiv \frac{\sqrt{-\nabla_\mu T \nabla^\mu T}}{\sqrt{\mathcal{I}(H^\perp)}},$$

where $\mathcal{I}(H^\perp)$ is a positive transverse curvature invariant. Admissibility requires $0 < \chi < \chi_{\max}$, with $\chi_{\max}$ set by vacuum stiffness and Machian sourcing. This bound replaces relativistic velocity limits in CFT: it constrains the rate of admissible reordering rather than motion through spacetime. Systems respond as rapidly as allowed by $\chi_{\max}$, which can be extremely large compared to macroscopic transport speeds while remaining finite and non-instantaneous [84].

It is crucial to distinguish this mechanism from quantum entanglement. In entanglement, correlations are encoded in a nonlocal wavefunction defined on a tensor product Hilbert space. In CFT, correlations arise because the ordering corridor already exists as a consequence of global matter sourcing. A local event does not transmit correlation; it selects among admissible configurations already constrained by the Machian functional. The resulting behavior may appear coordinated

across large distances, but it does not involve nonlocal state collapse or violation of finite-support evolution [85].

The same corridor logic applies across scales. In condensed-matter systems, rapid phase relocking following quenches or electromagnetic perturbations occurs along low-entropy ordering directions defined by lattice and electronic structure, as observed in ultrafast superconducting and charge-density-wave experiments [86]. In astrophysical systems, large-scale structural reconfiguration following mergers or collapses proceeds preferentially along filaments and planes defined by the global mass distribution, consistent with corridor-limited ordering rather than isotropic relaxation [87]. In each case, the observed rapidity reflects low transverse admissibility cost, not infinite propagation speed.

In summary, Machian ordering propagation in CFT is neither spacetime motion nor instantaneous influence. It is finite, corridor-limited reordering along longitudinal directions selected by global matter sourcing. The admissibility framework enforces continuity, finite support, and entropy constraints, while allowing rapid global coordination without invoking relativistic transport, quantum entanglement, or geometric dynamics of the metric. This establishes the physical meaning of Machian corridors as paths of least ordering resistance and prepares the ground for the subsequent discussion of exclusion, holonomy, and boundary-locked admissibility phenomena.

22 Conclusion

This work has established Chronoscalar Field Theory as a self-contained framework in which time is treated as a physical ordering scalar rather than as a passive parameter or coordinate label. From this starting point, the theory derives—rather than assumes—the existence of a Machian degrees-of-freedom split, finite-support admissibility, and a hierarchy of ordering responses that span atomic, condensed-matter, and astrophysical systems. At no stage is Riemannian geometry, spacetime curvature dynamics, or instantaneous influence invoked. The metric enters only as a kinematic bilinear for projection and bookkeeping, not as a dynamical object.

The Machian degrees-of-freedom split was shown to arise unavoidably from the existence of a timelike ordering gradient. Longitudinal variations along this gradient correspond to low-entropy streaming with minimal admissibility cost, while transverse variations correspond to shear, curvature microstructure, and entropy production. This split is mathematically enforced by projector algebra and the structure of the ordering Hessian, and it governs how systems resist, relax, and reorganize following perturbation. Inertia, within this framework, is not a fundamental property but an emergent resistance associated with transverse admissibility costs imposed by global matter sourcing.

Finite-support admissibility plays a central role throughout. By forbidding infinitesimal ordering histories and enforcing nonnegative ordering entropy production, the theory excludes instantaneous reconfiguration while allowing rapid global coordination. Apparent near-simultaneity in physical systems—ranging from lightning initiation and fracture dynamics to phase relocking and large-scale structure formation—is reinterpreted as relocking along pre-existing Machian ordering corridors. Nothing propagates through spacetime at superluminal speed; rather, systems reconfigure along corridors already selected by the global ordering field.

The theory further demonstrates that several phenomena traditionally treated as conceptually distinct—atomic orbital structure, NMR and ESR relaxation, Josephson phase coherence, Meissner exclusion, Aharonov–Bohm holonomy, Berry phase accumulation, and boundary-locked transport in topological materials—are unified as different diagnostics of the same underlying ordering manifold. Static imaging modes probe admissible geometry, relaxation experiments probe local relocking

stiffness, exclusion phenomena probe transverse admissibility collapse, and holonomy phenomena probe global corridor consistency. In each case, the observed behavior follows directly from admissibility constraints and the Machian sourcing of the ordering field.

Importantly, the framework produces concrete, testable scaling laws. The square-root acceleration behavior derived from transverse stiffness scaling is shown to arise as a stiffness-root law, not as a modification of Newtonian dynamics or a relativistic correction. The same formalism predicts specific dependencies of relaxation times, critical currents, coherence lengths, and anisotropy responses on curvature invariants and corridor structure. These predictions are quantitative and falsifiable, and they connect directly to existing experimental literature across multiple domains.

In summary, Chronoscalar Field Theory provides a consistent redefinition of relativity in which ordering, not spacetime geometry, is fundamental. General Relativity emerges as a coarse, symmetric limit of a deeper asymmetric ordering theory, valid when admissibility costs are isotropic and longitudinal dominance masks transverse structure. By restoring time asymmetry, finite support, and Machian global sourcing at the foundational level, CFT resolves longstanding conceptual tensions between inertia, causality, and coordination without introducing new forces, hidden variables, or nonphysical mechanisms. The theory therefore offers a coherent path forward for unifying microscopic ordering, macroscopic dynamics, and cosmological structure within a single admissibility-governed framework.[89]

References

1. C. A. Grant, "Chronoscalar Field Theory Corpus," *AIXIV*, available under the range of IDs: `aixiv:251201.000001` to `aixiv:251222.000005` (2025).

3. J. D. Jackson, *Classical Electrodynamics*, 3rd ed. (Wiley, New York, 1998).

4. P. A. M. Dirac, *The Principles of Quantum Mechanics*, 4th ed. (Oxford University Press, Oxford, 1958).

5. E. Schrödinger, "Quantisierung als Eigenwertproblem," *Annalen der Physik* **384**, 361–376 (1926).

6. J. von Neumann, *Mathematical Foundations of Quantum Mechanics* (Princeton University Press, Princeton, 1955).

7. A. Einstein, "Zur Elektrodynamik bewegter Körper," *Annalen der Physik* **322**, 891–921 (1905).

8. L. D. Landau and E. M. Lifshitz, *Quantum Mechanics: Non-Relativistic Theory*, 3rd ed. (Pergamon Press, Oxford, 1977).

9. W. Demtröder, *Atoms, Molecules and Photons* (Springer, Berlin, 2006).

10. P. Strange, *Relativistic Quantum Mechanics* (Cambridge University Press, Cambridge, 1998).

11. M. V. Berry, "Quantal phase factors accompanying adiabatic changes," *Proc. R. Soc. Lond. A* **392**, 45–57 (1984).

12. S. V. Eremeev, I. A. Nechaev, Y. M. Koroteev, *et al.*, "Atom-specific spin mapping and buried topological states in W(110)," *Nature Communications* **3**, 635 (2012).

13. A. Varykhalov, J. Sánchez-Barriga, A. M. Shikin, *et al.*, "Electronic and magnetic properties of surface states in tungsten," *Phys. Rev. Lett.* **101**, 157601 (2008).

14. E. M. Purcell, H. C. Torrey, and R. V. Pound, "Resonance absorption by nuclear magnetic moments in a solid," *Phys. Rev.* **69**, 37–38 (1946).

15. F. Bloch, W. W. Hansen, and M. Packard, "Nuclear induction," *Phys. Rev.* **69**, 127 (1946).

16. A. Abragam, *The Principles of Nuclear Magnetism* (Oxford University Press, Oxford, 1961).

17. C. P. Slichter, *Principles of Magnetic Resonance*, 3rd ed. (Springer, Berlin, 1990).

18. R. R. Ernst, G. Bodenhausen, and A. Wokaun, *Principles of Nuclear Magnetic Resonance in One and Two Dimensions* (Oxford University Press, Oxford, 1987).

19. M. Mehring, *High Resolution NMR Spectroscopy in Solids* (Springer, Berlin, 1983).

20. A. G. Redfield, "The theory of relaxation processes," *Adv. Magn. Reson.* **1**, 1–32 (1965).

21. F. Bloch, "Nuclear induction," *Phys. Rev.* **70**, 460–474 (1946).

22. A. G. Redfield, "On the theory of relaxation processes," *IBM J. Res. Dev.* **1**, 19–31 (1957).

23. A. Abragam, *The Principles of Nuclear Magnetism* (Oxford University Press, Oxford, 1961).

24. C. P. Slichter, *Principles of Magnetic Resonance*, 3rd ed. (Springer, Berlin, 1990).

25. N. Bloembergen, E. M. Purcell, and R. V. Pound, "Relaxation effects in nuclear magnetic resonance absorption," *Phys. Rev.* **73**, 679–712 (1948).

26. A. M. Tyryshkin, S. Tojo, J. J. L. Morton, *et al.*, "Electron spin coherence exceeding seconds in high-purity silicon," *Nature Materials* **11**, 143–147 (2012).

27. F. Bloch, "Nuclear induction," *Phys. Rev.* **70**, 460–474 (1946).

28. A. G. Redfield, "On the theory of relaxation processes," *IBM J. Res. Dev.* **1**, 19–31 (1957).

29. N. Bloembergen, E. M. Purcell, and R. V. Pound, "Relaxation effects in nuclear magnetic resonance absorption," *Phys. Rev.* **73**, 679–712 (1948).

30. A. Abragam, *Principles of Nuclear Magnetism* (Oxford University Press, Oxford, 1961).

31. C. P. Slichter, *Principles of Magnetic Resonance*, 3rd ed. (Springer, Berlin, 1990).

32. R. Tycko, S. E. Barrett, G. Dabbagh, L. N. Pfeiffer, and K. W. West, "Electronic states in crystalline silicon studied by high-resolution ^{29}Si NMR," *Phys. Rev. Lett.* **64**, 2583–2586 (1990).

33. C. P. Poole, *Electron Spin Resonance*, 2nd ed. (Wiley, New York, 1983).

34. A. Abragam and B. Bleaney, *Electron Paramagnetic Resonance of Transition Ions* (Oxford University Press, Oxford, 1970).

35. J. H. Van Vleck, *The Theory of Electric and Magnetic Susceptibilities* (Oxford University Press, Oxford, 1932).

36. M. Hoesch *et al.*, "Spin structure of the Shockley surface state on Au(111)," *Phys. Rev. B* **69**, 241401 (2004).

37. R. Kubo, "The fluctuation–dissipation theorem," *Rep. Prog. Phys.* **29**, 255–284 (1966).

38. S. LaShell, B. A. McDougall, and E. Jensen, "Spin splitting of an Au(111) surface state band," *Phys. Rev. Lett.* **77**, 3419–3422 (1996).

39. M. V. Berry, "Quantal phase factors accompanying adiabatic changes," *Proc. R. Soc. Lond. A* **392**, 45–57 (1984).

40. N. Nagaosa *et al.*, "Anomalous Hall effect," *Rev. Mod. Phys.* **82**, 1539–1592 (2010).

41. M. Hoesch *et al.*, "Spin structure of the Shockley surface state on Au(111)," *Phys. Rev. B* **69**, 241401 (2004).

42. N. Nagaosa, J. Sinova, S. Onoda, A. H. MacDonald, and N. P. Ong, "Anomalous Hall effect," *Rev. Mod. Phys.* **82**, 1539–1592 (2010).

43. B. D. Josephson, "Possible new effects in superconductive tunnelling," *Phys. Lett.* **1**, 251–253 (1962).

44. W. C. Stewart, "Current–voltage characteristics of Josephson junctions," *Appl. Phys. Lett.* **12**, 277–280 (1968).

45. D. E. McCumber, "Effect of ac impedance on dc voltage–current characteristics of superconductor weak-link junctions," *J. Appl. Phys.* **39**, 3113–3118 (1968).

46. A. Barone and G. Paternò, *Physics and Applications of the Josephson Effect* (Wiley, New York, 1982).

47. M. Tinkham, *Introduction to Superconductivity*, 2nd ed. (McGraw–Hill, New York, 1996).

48. D. J. Van Harlingen, "Phase-sensitive tests of the symmetry of the pairing state in the high-temperature superconductors," *Rev. Mod. Phys.* **67**, 515–535 (1995).

49. Y. Aharonov and D. Bohm, "Significance of electromagnetic potentials in the quantum theory," *Phys. Rev.* **115**, 485–491 (1959).

50. C. C. Tsuei and J. R. Kirtley, "Pairing symmetry in cuprate superconductors," *Rev. Mod. Phys.* **72**, 969–1016 (2000).

51. W. Meissner and R. Ochsenfeld, "Ein neuer Effekt bei Eintritt der Supraleitfähigkeit," *Naturwissenschaften* **21**, 787–788 (1933).

52. F. London and H. London, "The electromagnetic equations of the supraconductor," *Proc. R. Soc. Lond. A* **149**, 71–88 (1935).

53. M. Tinkham, *Introduction to Superconductivity*, 2nd ed. (McGraw–Hill, New York, 1996).

54. R. Prozorov and R. W. Giannetta, "Magnetic penetration depth in unconventional superconductors," *Supercond. Sci. Technol.* **19**, R41–R67 (2006).

55. J. Bardeen, L. N. Cooper, and J. R. Schrieffer, "Theory of superconductivity," *Phys. Rev.* **108**, 1175–1204 (1957).

56. R. Doll and M. Näbauer, "Experimental proof of magnetic flux quantization in a superconducting ring," *Phys. Rev. Lett.* **7**, 51–52 (1961).

57. J. R. Clem, "Penetration depth and coherence length in superconductors," in *Superconductivity*, Vol. 1, ed. R. D. Parks (Marcel Dekker, New York, 1969).

58. W. N. Hardy, D. A. Bonn, D. C. Morgan, R. Liang, and K. Zhang, "Precision measurements of the temperature dependence of λ in $YBa_2Cu_3O_{6.95}$," *Phys. Rev. Lett.* **70**, 3999–4002 (1993).

59. D. N. Basov and T. Timusk, "Electrodynamics of high-T_c superconductors," *Rev. Mod. Phys.* **77**, 721–779 (2005).

60. Y. Aharonov and D. Bohm, "Significance of electromagnetic potentials in the quantum theory," *Phys. Rev.* **115**, 485–491 (1959).

61. R. G. Chambers, "Shift of an electron interference pattern by enclosed magnetic flux," *Phys. Rev. Lett.* **5**, 3–5 (1960).

62. M. Peshkin and A. Tonomura, *The Aharonov–Bohm Effect* (Springer, Berlin, 1989).

63. A. Tonomura, N. Osakabe, T. Matsuda, T. Kawasaki, J. Endo, S. Yano, and H. Yamada, "Evidence for Aharonov–Bohm effect with magnetic field completely shielded from electron wave," *Phys. Rev. Lett.* **56**, 792–795 (1986).

64. S. Washburn and R. A. Webb, "Aharonov–Bohm effect in normal metal quantum coherence and transport," *Adv. Phys.* **35**, 375–422 (1986).

65. M. V. Berry, "Quantal phase factors accompanying adiabatic changes," *Proc. R. Soc. Lond. A* **392**, 45–57 (1984).

66. Y. Imry, *Introduction to Mesoscopic Physics*, 2nd ed. (Oxford University Press, Oxford, 2002).

67. B. L. Altshuler, A. G. Aronov, and D. E. Khmelnitskii, "Effects of electron–electron collisions with small energy transfers on quantum localisation," *J. Phys. C* **15**, 7367–7386 (1982).

68. H. van Houten, C. W. J. Beenakker, and A. A. M. Staring, "Quantum transport in semiconductor nanostructures," in *Single Charge Tunneling*, eds. H. Grabert and M. H. Devoret (Plenum, New York, 1992).

69. M. Z. Hasan and C. L. Kane, "Colloquium: Topological insulators," *Rev. Mod. Phys.* **82**, 3045–3067 (2010).

70. X.-L. Qi and S.-C. Zhang, "Topological insulators and superconductors," *Rev. Mod. Phys.* **83**, 1057–1110 (2011).

71. Y. Xia, D. Qian, D. Hsieh, L. Wray, A. Pal, *et al.*, "Observation of a large-gap topological-insulator class with a single Dirac cone on the surface," *Nat. Phys.* **5**, 398–402 (2009).

72. Y. L. Chen, J. G. Analytis, J.-H. Chu, Z. K. Liu, *et al.*, "Massive Dirac fermion on the surface of a magnetically doped topological insulator," *Science* **329**, 659–662 (2010).

73. H. Zhang, C.-X. Liu, X.-L. Qi, X. Dai, Z. Fang, and S.-C. Zhang, "Topological insulators in Bi_2Se_3, Bi_2Te_3 and Sb_2Te_3 with a single Dirac cone on the surface," *Nat. Phys.* **5**, 438–442 (2009).

74. P. Dziawa, B. J. Kowalski, K. Dybko, R. Buczko, *et al.*, "Topological crystalline insulator states in $Pb_{1-x}Sn_xSe$," *Nat. Mater.* **11**, 1023–1027 (2012).

75. J. Wang, B. Lian, and S.-C. Zhang, "Quantum anomalous Hall effect in magnetic topological insulators," *Phys. Rev. B* **89**, 085106 (2014).

76. J. Dalibard, F. Gerbier, G. Juzeliūnas, and P. Öhberg, "Colloquium: Artificial gauge potentials for neutral atoms," *Rev. Mod. Phys.* **83**, 1523–1543 (2011).

77. N. Goldman, G. Juzeliūnas, P. Öhberg, and I. B. Spielman, "Light-induced gauge fields for ultracold atoms," *Rep. Prog. Phys.* **77**, 126401 (2014).

78. M. Aidelsburger, M. Atala, S. Nascimbène, S. Trotzky, Y.-A. Chen, and I. Bloch, "Realization of the Hofstadter Hamiltonian with ultracold atoms in optical lattices," *Phys. Rev. Lett.* **111**, 185301 (2013).

79. H. Miyake, G. A. Siviloglou, C. J. Kennedy, W. C. Burton, and W. Ketterle, "Realizing the Harper Hamiltonian with laser-assisted tunneling in optical lattices," *Phys. Rev. Lett.* **111**, 185302 (2013).

80. M. Z. Hasan and C. L. Kane, "Colloquium: Topological insulators," *Rev. Mod. Phys.* **82**, 3045–3067 (2010).

81. X.-L. Qi and S.-C. Zhang, "Topological insulators and superconductors," *Rev. Mod. Phys.* **83**, 1057–1110 (2011).

82. L. Fu, C. L. Kane, and E. J. Mele, "Topological insulators in three dimensions," *Phys. Rev. Lett.* **98**, 106803 (2007).

83. D. Hsieh, D. Qian, L. Wray, Y. Xia, Y. S. Hor, *et al.*, "A topological Dirac insulator in a quantum spin Hall phase," *Nature* **452**, 970–974 (2008).

84. Y. Xia *et al.*, "Observation of a large-gap topological-insulator class with a single Dirac cone on the surface," *Nat. Phys.* **5**, 398–402 (2009).

85. P. Roushan *et al.*, "Topological surface states protected from backscattering by chiral spin texture," *Nature* **460**, 1106–1109 (2009).

86. J. E. Moore, "The birth of topological insulators," *Nature* **464**, 194–198 (2010).

87. A. P. Schnyder, S. Ryu, A. Furusaki, and A. W. W. Ludwig, "Classification of topological insulators and superconductors," *Phys. Rev. B* **78**, 195125 (2008).

88. C. L. Kane and E. J. Mele, "Z_2 topological order and the quantum spin Hall effect," *Phys. Rev. Lett.* **95**, 146802 (2005).

89. H. Bondi and J. Samuel, "The Lense–Thirring effect and Mach's principle," *Phys. Lett. A* **228**, 121–126 (1997). .

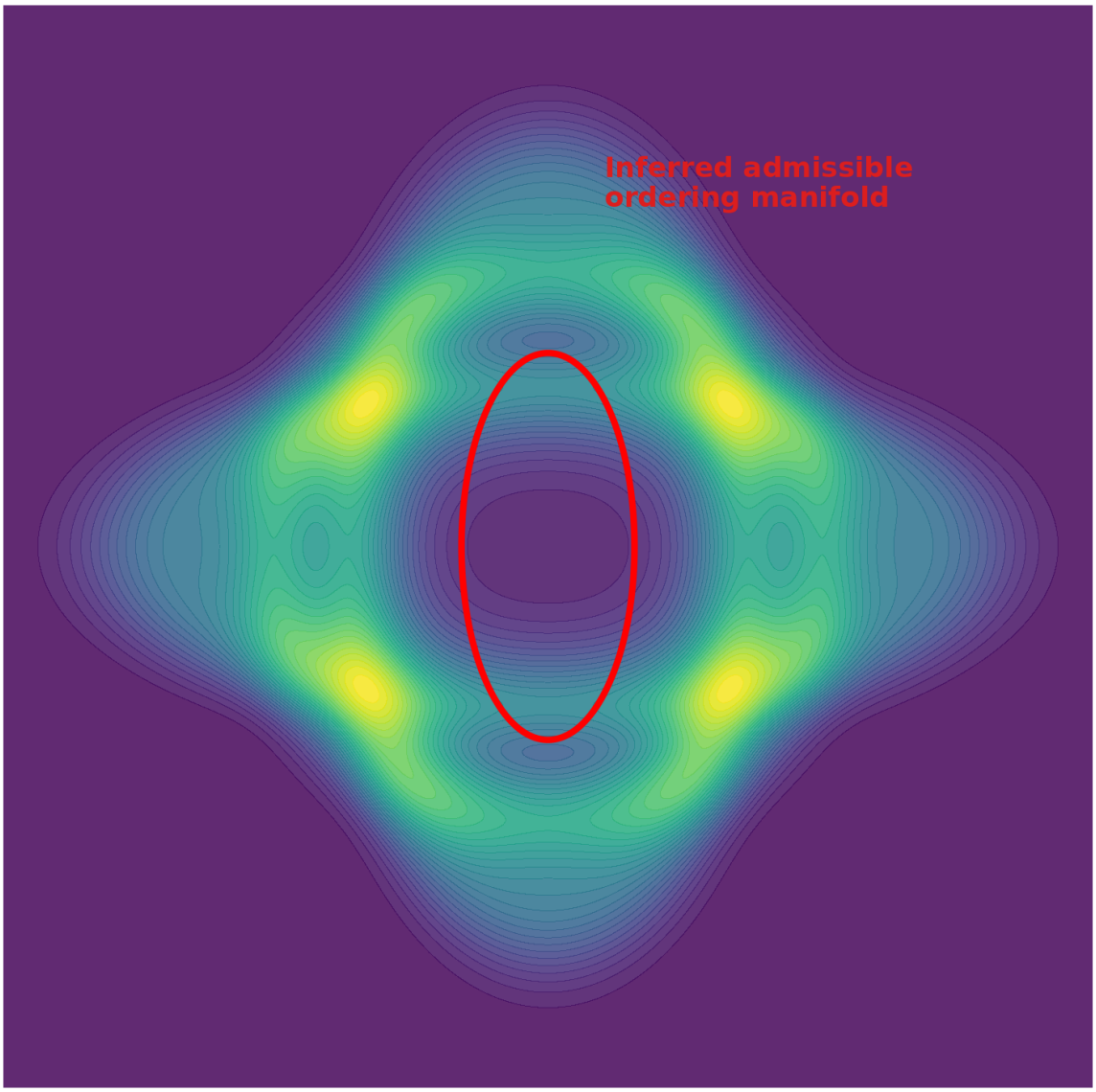

Figure 1: Schematic representation of concurrent atomic shell structure in real space. Multiple subshells overlap strongly in radius and angle, producing anisotropy while obscuring the dominant ordering directions. Real-space diagnostics capture confinement and nodal structure but cannot uniquely determine the underlying ordering manifold geometry when shells are concurrent.

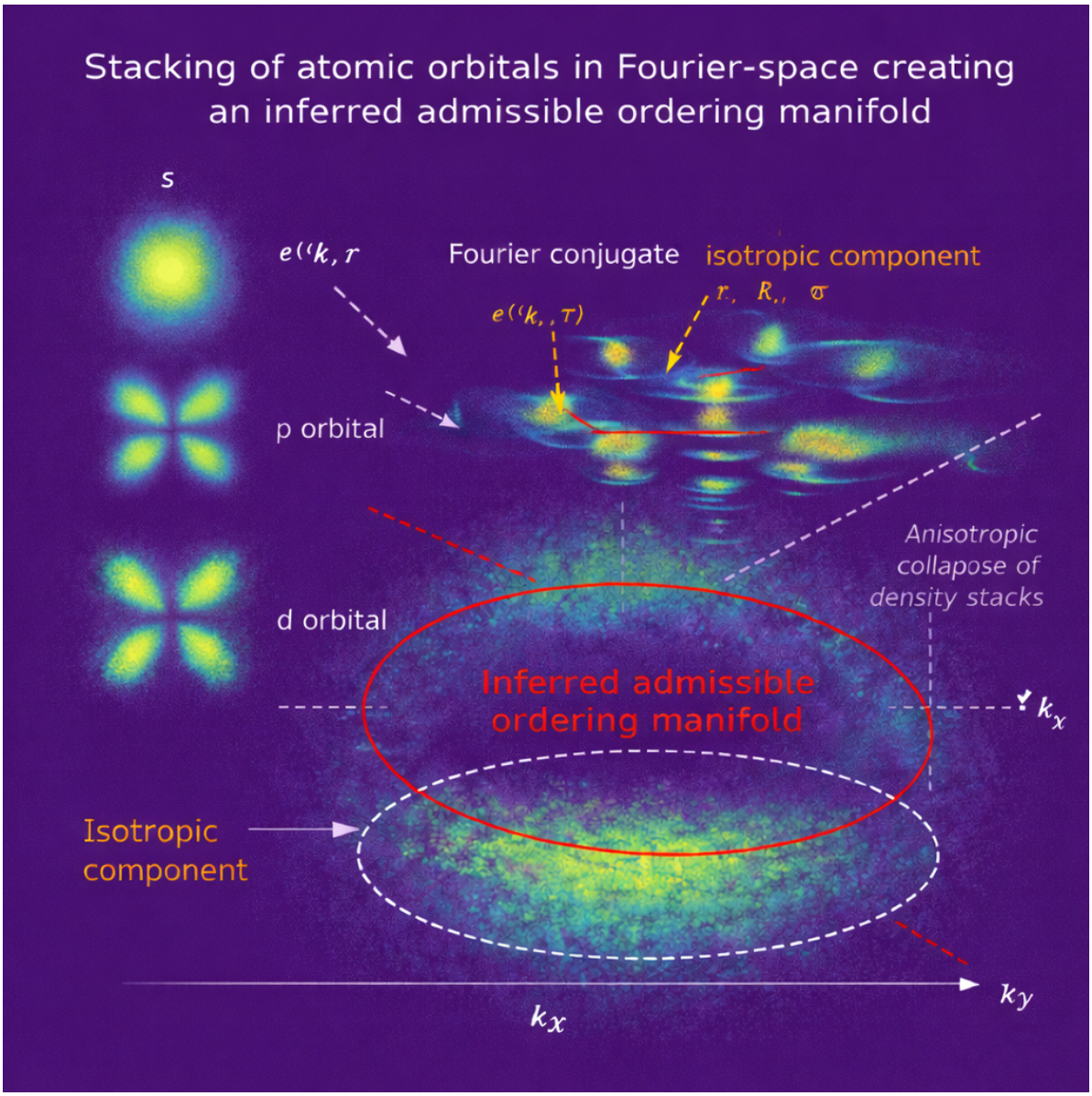

Figure 2: Fourier-space reconstruction of the concurrent tungsten shell manifold. (a) Spectral power density $|\tilde{\rho}(\mathbf{k})|^2$ showing anisotropic collapse of shell concurrency. (b) Principal-axis decomposition revealing dominance of two ordering directions and suppression of the third. (c) Projection of the resulting spectral sheet, which defines the admissible transport surface observed experimentally.

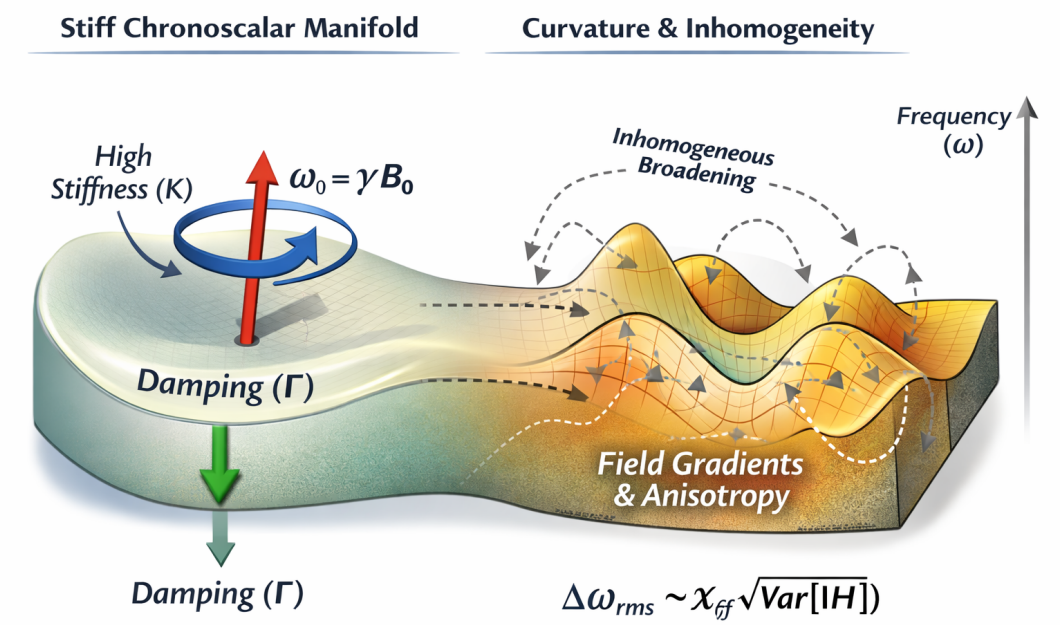

Figure 3: High-magnification view of the local admissible ordering manifold governing NMR dynamics. The nuclear spin precesses according to the right-hand rule about the external field $\mathbf{B}_0$, while the surrounding electronic and lattice environment defines a curved chronoscalar manifold with anisotropic stiffness. The illustrated scale corresponds to a mesoscopic ordering volume: larger than an individual electronic orbital but smaller than a crystallographic unit cell, such that shell concurrency, dipolar geometry, and local Hessian variation are simultaneously resolved. Longitudinal relaxation (T_1) corresponds to slow relocking of the ordering coordinate along the stiff manifold direction, controlled by the stiffness K and damping Γ. Transverse dephasing and linewidth broadening arise from spatial variation of the local Hessian $H_{ij} = \nabla_i \nabla_j T$, which produces orientation-dependent frequency offsets $\Delta\omega_{\text{rms}}$. This geometric separation visually encodes Eqs. (27)–(35), explaining how a system may exhibit very long T_1 while simultaneously showing rapid loss of phase coherence.